JCB Journal of Cell Biology

ARTICLE

Binding and transport of SFPQ-RNA granules by KIF5A/KLC1 motors promotes axon survival

Yusuke Fukuda[1,2], Maria F. Pazyra-Murphy[1,2], Elizabeth S. Silagi[1,2], Ozge E. Tasdemir-Yilmaz[1,2], Yihang Li[1,2], Lillian Rose[1,2], Zoe C. Yeoh[2], Nicholas E. Vangos[2], Ezekiel A. Geffken[2], Hyuk-Soo Seo[2,3], Guillaume Adelmant[2,4,5,6], Gregory H. Bird[2,7,8], Loren D. Walensky[2,7,8], Jarrod A. Marto[2,4,5,6], Sirano Dhe-Paganon[2,3], and Rosalind A. Segal[1,2]

Complex neural circuitry requires stable connections formed by lengthy axons. To maintain these functional circuits, fast transport delivers RNAs to distal axons where they undergo local translation. However, the mechanism that enables long-distance transport of RNA granules is not yet understood. Here, we demonstrate that a complex containing RNA and the RNA-binding protein (RBP) SFPQ interacts selectively with a tetrameric kinesin containing the adaptor KLC1 and the motor KIF5A. We show that the binding of SFPQ to the KIF5A/KLC1 motor complex is required for axon survival and is impacted by KIF5A mutations that cause Charcot-Marie Tooth (CMT) disease. Moreover, therapeutic approaches that bypass the need for local translation of SFPQ-bound proteins prevent axon degeneration in CMT models. Collectively, these observations indicate that KIF5A-mediated SFPQ-RNA granule transport may be a key function disrupted in *KIF5A*-linked neurologic diseases and that replacing axonally translated proteins serves as a therapeutic approach to axonal degenerative disorders.

Introduction

Sensory and motor neurons transmit signals along axons than can exceed 1 meter in length; therefore, many axonal functions, including axonal survival pathways, depend on proteins that are locally translated and replenished in axon terminals (Holt et al., 2019). Localized protein synthesis is enabled by the initial assembly of mRNAs and RNA-binding proteins (RBPs) into RNP granules that occurs within the cell soma, the transport of these RNA granules to axon endings, and the subsequent release of RNA for local protein synthesis (Das et al., 2019; Sahoo et al., 2018). Human mutations affecting RBPs, cytoskeletal components, or intracellular motors are a major cause of neurologic diseases, including amyotrophic lateral sclerosis (ALS), hereditary spastic paraplegia, and Charcot-Marie Tooth (CMT) disease (Nussbacher et al., 2019; Sleigh et al., 2019). Degeneration of axons occurs early in such neurodegenerative disorders and precedes cell death of the affected neurons (Krauss et al., 2020; Salvadores et al., 2017); however, it is not yet known which components must be transported to maintain healthy axons.

The large family of kinesin motors enables anterograde axonal transport, and the genes encoding kinesins are frequently mutated in neurodegenerative disorders. Three distinct genes—*KIF5A, KIF5B*, and *KIF5C*—encode the conventional kinesin-1 family of motors (Xia et al., 1998), which transport RNP granules, vesicles, and other organelles in an anterograde direction toward axon terminals. Although KIF5 motors are highly similar at the sequence and structural level, neurodegenerative disorders are predominantly associated with *KIF5A*. Mutations in the motor domain of KIF5A affect microtubule binding and/or ATP hydrolysis, leading to sensory degeneration in CMT2 or motor symptoms in hereditary spastic paraplegia, while mutations affecting the cargo-binding region of KIF5A cause ALS (Dutta et al., 2018; Ebbing et al., 2008; Füger et al., 2012; Jennings et al., 2017; Brenner et al., 2018; Nicolas et al., 2018). The distinctive involvement of *KIF5A* mutations in neurologic disease could reflect differential expression patterns of KIF5A compared with other KIF5 isoforms and/or critical cargos that selectively require KIF5A for transport.

Previous studies have identified some functional specificity among the KIF5 motors. KIF5B regulates dendritic transport of synaptic components in hippocampal neurons (Zhao et al., 2020). Additional dendritic cargos specifically transported by KIF5A include γ-aminobutyric acid A ($GABA_A$) receptor–associated protein (Nakajima et al., 2012). Splicing factor proline/glutamine-rich (SFPQ) is a ubiquitous RBP that has critical functions in axons of

---

[1]Department of Neurobiology, Harvard Medical School, Boston, MA; [2]Department of Cancer Biology, Dana-Farber Cancer Institute, Boston, MA; [3]Department of Biological Chemistry and Molecular Pharmacology, Harvard Medical School, Boston, MA; [4]Blais Proteomics Center, Dana-Farber Cancer Institute, Boston, MA; [5]Department of Oncologic Pathology, Dana-Farber Cancer Institute, Boston, MA; [6]Department of Pathology, Brigham and Women's Hospital and Harvard Medical School, Boston, MA; [7]Linde Program in Cancer Chemical Biology, Dana-Farber Cancer Institute, Boston, MA; [8]Department of Pediatric Oncology, Dana-Farber Cancer Institute, Boston, MA.

Correspondence to Rosalind A. Segal: rosalind_segal@dfci.harvard.edu.

Rockefeller University Press
J. Cell Biol. 2020 Vol. 220 No. 1 e202005051
https://doi.org/10.1083/jcb.202005051

both sensory and motor neurons (Cosker et al., 2016; Pease-Raissi et al., 2017; Thomas-Jinu et al., 2017). In sensory neurons, SFPQ assembles neurotrophin-regulated transcripts, such as *bclw* and *lmnb2*, to form RNP granules (Cosker et al., 2016) and is required for axonal localization of these mRNAs and their subsequent translation to exert their prosurvival functions (Cioni et al., 2019; Cosker et al., 2013; Courchesne et al., 2011; Yoon et al., 2012; Pease-Raissi et al., 2017). Similar to many other RBPs, SFPQ contains an intrinsically disordered region (Fig. S1 A) and has been demonstrated to be a component of large RNP transport granules in neurons (Kanai et al., 2004). Thus, loss of SFPQ leads to the depletion of axonal mRNAs and results in axon degeneration in dorsal root ganglion (DRG) sensory neurons (Cosker et al., 2016). Similarly, SFPQ is critical for the development and maintenance of motor neuron axons (Thomas-Jinu et al., 2017). Missense mutations in the coiled-coil region of SFPQ have been identified that cause familial ALS and impair the localization of SFPQ within distal axon segments (Thomas-Jinu et al., 2017). However, we do not yet understand the mechanisms by which this RBP organizes mRNA transport granules that can then move rapidly to distal axons where mRNA cargos are released and translated.

Here, we show that SFPQ binds preferentially to a kinesin motor containing KIF5A in association with its adaptor kinesin light chain (KLC) 1 (KLC1). Disruption of SFPQ binding to KIF5A-KLC1 motors impedes transport of RNP granules and triggers axon degeneration. Moreover, our data suggest that axonal degeneration in sensory neurons caused by *KIF5A* mutations that are typical of CMT2 can be prevented by a Bclw peptide that bypasses axonal functions of SFPQ. Together, these data reveal that specialized kinesin motors composed of KIF5A and KLC1 transport SFPQ-RNA granules along the axons, and defects in the KIF5A-dependent motility of SFPQ-RNA granules cause axonal degeneration, which contributes to sensory neuropathy in CMT2.

Results

SFPQ-containing transport granules move in a bidirectional manner in axons of DRG sensory neurons

The RBP SFPQ is found in both cell bodies (CBs) and axons of sensory neurons; however, the mechanisms by which SFPQ and its critical RNA cargos are transported between these two locations is not known. We used live cell imaging of DRG sensory neurons expressing Halo-tagged SFPQ to directly visualize transport dynamics (Video 1). Fluorescent signal was enriched in the nucleus and was also evident as discrete granules in the soma and axons, a pattern similar to the distribution of endogenous SFPQ (Cosker et al., 2016). Consistent with the presence of an intrinsically disordered region within the SFPQ coding sequence (Fig. S1 A), Halo-tagged SFPQ granules exhibited liquid-like properties during time-lapse imaging. The size and shape of SFPQ granules remained constant at ~1 µm in diameter during the stationary phase, while the granules expanded and elongated as they moved (Fig. 1, A and B). The majority of the Halo-tagged SFPQ granules in axons were motile, either moving by retrograde transport (~50%) or anterograde transport (~23%), with the remainder in stationary phase (~27%; Fig. 1, C and D). SFPQ granules exhibit an average anterograde velocity of 0.85 ± 0.07 µm/s and an average anterograde run length of 21.50 ± 2.22 µm, with an average retrograde velocity of 0.79 ± 0.04 µm/s and average retrograde run length of 30.45 ± 1.94 µm (Fig. 1, E and F; and Fig. S1, B and C). Together, the velocity and characteristics of movement indicate that the SFPQ-containing transport granules move in both directions by microtubule-dependent fast axonal transport using a kinesin motor for anterograde movements and the more highly processive dynein motor for retrograde movements.

SFPQ preferentially binds to KIF5A/KLC1 in DRG sensory neurons

The anterograde kinesins involved in axon transport are formed by a dimer of kinesin heavy chain (KHC or KIF5) complexed with a dimer of KLC (Fig. 2 A; Hirokawa et al., 2010). The *KIF5* family is encoded by three distinct genes—*KIF5A*, *KIF5B*, and *KIF5C*—and the genome also contains several light chains, *KLC1–4*. To identify motors that associate with SFPQ and that might enable transport of these RNP granules, we immunoprecipitated endogenous SFPQ from DRG neurons and analyzed the coprecipitated protein by mass spectrometry. In addition to known interactors of SFPQ, such as *Drosophila* behavior/human splicing protein family members NONO and PSPC1, we detected several components of the KLC and KIF motor complex among the coprecipitated proteins (Data S1). We then used a targeted mass spectrometry approach to quantify the relative abundance of KIF5A, KIF5B, and KIF5C (Fig. 2 B), as well as KLC1 and KLC2 (Fig. 2 C) associated with the immunoprecipitated SFPQ. We found that KIF5A and KLC1 were approximately twice as abundant compared with KIF5B or KIF5C and KLC2, respectively, as measured across three independent experiments (Fig. 2, B and C).

By using validated antibodies specific to each of the three KIF5s (Fig. S2, A and B), we corroborated that SFPQ preferentially coimmunoprecipitates with KIF5A, rather than the closely related KIF5B or KIF5C (Fig. 2, D and E), as well as with KLC1 rather than KLC2 (Fig. 2 F). We further addressed the specificity of this interaction by testing other kinesins that were identified with mass spectrometry in the coprecipitates of SFPQ: KIF1A, KIF3C, and KIF3A (Data S1). KIF1A is a major axonal transport motor protein in DRGs (Tanaka et al., 2016), whereas KIF3A and KIF3C function in transporting RNA granules in neurons (Baumann et al., 2014; Davidovic et al., 2007). However, none of these kinesins significantly coimmunoprecipitates with SFPQ when tested using antibodies specific to these kinesins (Fig. S2 C).

Interestingly, the KLC1 that immunoprecipitates with SFPQ exhibited a shift in apparent molecular weight compared with the total KLC1 present in the input (Fig. 2 F), suggesting potential posttranslation modification of KLC1. We asked whether KLC1 is phosphorylated in DRG neurons by treating DRG lysates with intestinal alkaline phosphatase. Treatment of lysates with intestinal alkaline phosphatase shifted KLC1 to a band of lower apparent molecular weight, indicative of its phosphorylation (Fig. S2 D). Intriguingly, neurotrophins, which play a critical

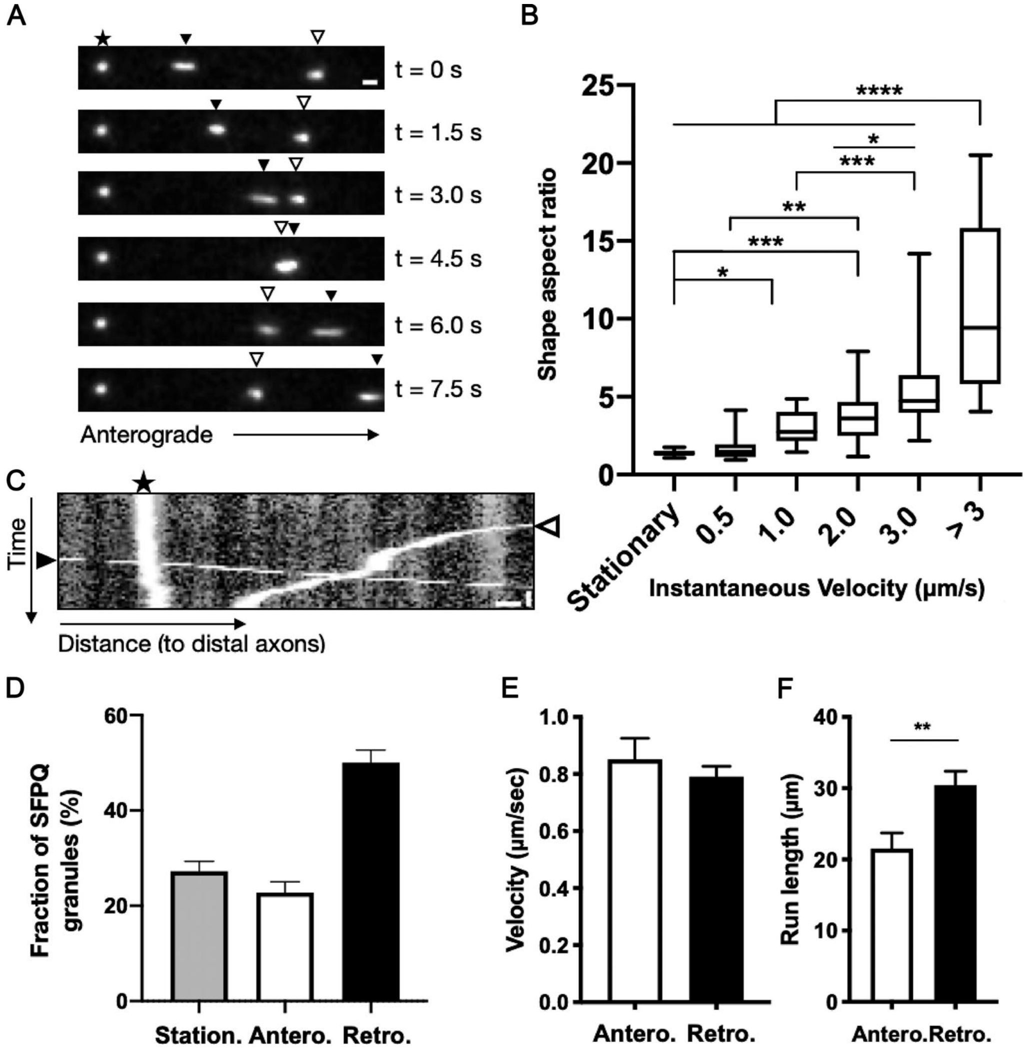

Figure 1. **SFPQ-containing transport granules move in a bidirectional manner in axons of DRG sensory neurons. (A)** Time lapse images of Halo-SFPQ in stationary (star), anterograde (closed arrowhead), and retrograde phase (open arrowhead). Scale bar: 1.2 μm. **(B)** Shape aspect ratio (maximum diameter/minimum diameter) of SFPQ granules calculated for stationary and moving granules, categorized with their instantaneous velocities as indicated. Data are calculated from 24 SFPQ granules from five axons from five independent microfluidic experiments for time points in stationary (*n* = 28), ≤0.5 (*n* = 33), 0.5–1 (*n* = 28), 1–2 (*n* = 28), 2–3 (*n* = 25), and >3 μm/s (*n* = 11). ****P < 0.0001; ***P = 0.0003; **P = 0.0018; *P = 0.0354, 0.0308 with one-way ANOVA. **(C)** Kymograph depicting Halo-SFPQ in stationary (star), anterograde (closed arrowhead), and retrograde (open arrowhead) phase. Scale bars: 2 μm and 9 s. **(D)** Fraction of SFPQ granules spent in stationary, anterograde, or retrograde phase. **(E and F)** Average velocity (E) and average run length (F) of Halo-tagged SFPQ granules in axons for anterograde and retrograde transport. **P = 0.0032 by unpaired two-paired *t* test; data represent mean ± SEM. Data from D, E, and F are analyzed from 259 SFPQ particles from 34 axons across four independent microfluidic experiments.

role in the development and survival of DRG neurons (Huang and Reichardt, 2001), also regulate phosphorylation of KLC1. Neurotrophin stimulation results in KLC1 shifting to a band of lower molecular weight, which is indicative of the dephosphorylation of KLC1 (Fig. S2 E), suggesting that target-derived neurotrophins may regulate the binding of KIF5A/KLC1 motors to SFPQ, thereby causing SFPQ granules to be released from kinesin motors in distal axons. Together, these results suggest that KIF5A/KLC1 tetramers constitute the major motor responsible for anterograde axonal transport of SFPQ to the axon terminals.

A previous study of kinesin-1 motors demonstrates that overexpressed KIF5A, -B, and -C can all traffic to axons, but KIF5A is excluded from dendrites (Lipka et al., 2016). DRG sensory neurons are pseudounipolar in morphology and so have no dendrites, but instead consist of a CB with a T-shaped axon. To determine whether the intracellular distribution of kinesins is consistent with the hypothesis that the KIF5A/KLC1 motor transports SFPQ-RNA granules, we cultured DRG sensory neurons in compartmented cultures and collected protein lysates distinctly from CB and distal axon compartments (Fig. 2 G). While KIF5B preferentially localizes in the CB compartment, KIF5A and KIF5C localize to both CB and distal axon compartments, as do KLC1 and KLC2 (Fig. 2, H and I). Immunostaining of KIF5s in DRG neurons that were cultured in microfluidic chambers as well as DRGs and sciatic nerves in vivo displayed a similar localization pattern, with KIF5B largely excluded from axons (Fig. S2, F and G). Together, these data demonstrate that

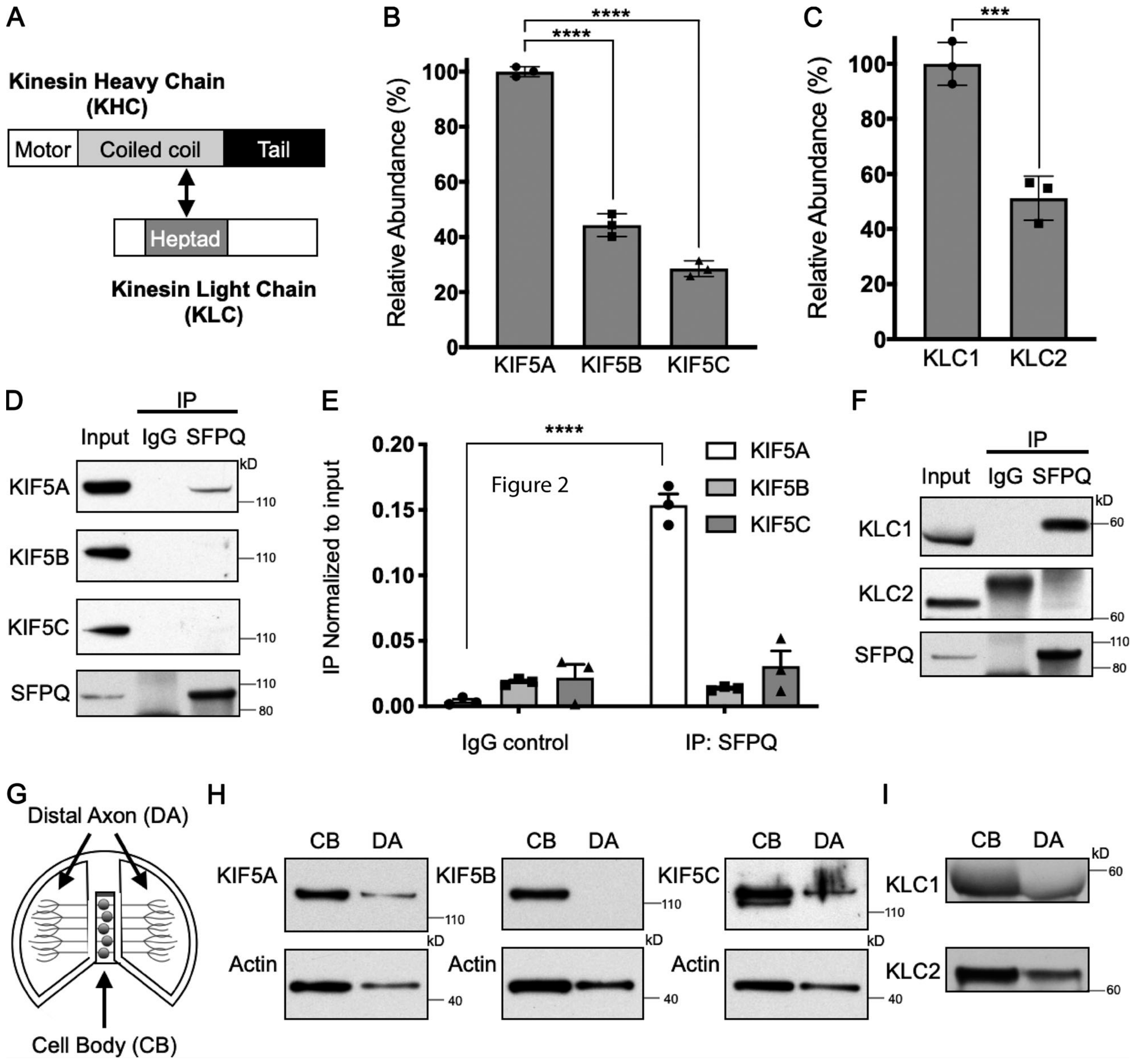

Figure 2. **SFPQ preferentially binds to KIF5A/KLC1 in DRG sensory neurons. (A)** Schematic of domains for kinesin heavy chain (KHC) and KLC and their interacting region between the coiled coil of KHC and with the heptad repeat of KLC. **(B)** PRM-based quantification of KIF5A, KIF5B, and KIF5C in SFPQ immunoprecipitations. Error bars represent SD, n = 3; ****$P < 0.001$; 95% CIs for the difference in means (KIF5A; KIF5B: 47.0-64.3%; and KIF5A; KIF5C: 65.7-77.2%), Welch two-sample t test. **(C)** PRM-based quantification of KLC1 and KLC2 in SFPQ immunoprecipitations. Error bars represent SD, n = 3; ***$P < 0.05$, 95% CI for the difference in means (KLC1-KLC2: 30.9-66.7%), Welch two-sample t test. **(D)** IP of endogenous SFPQ from DRG sensory neuron protein lysate and blotted against endogenous KIF5A, KIF5B, and KIF5C. IgG serves as control IP, input represents 3% of 0.5 mg of protein lysate used for SFPQ IP, and total elute from the bead was run on the gel. **(E)** Quantification of pull down in D relative to input. ****$P < 0.0001$ by two-way ANOVA; n = 3 independent IPs; data represent mean ± SEM. **(F)** IP of endogenous SFPQ from DRG sensory neuron protein lysate and blotted against endogenous KLC1 and KLC2. IgG serves as control IP, input represents 3% of 0.5 mg of protein lysate used for SFPQ IP, and total elute from the bead was run on the gel. **(G)** Schematic representation of DRG sensory neurons grown in compartmented Campenot culture for preparing protein lysates for Western blot. **(H and I)** Western blot of DRG neuron lysates of CB and distal axon (DA) prepared from compartmented Campenot cultures probed against endogenous KIF5 motors (H) and KLCs (I); actin serves as loading control for H.

KIF5A and KLC1 are appropriately localized to mediate the transport of SFPQ-RNA granules from CBs to distal axons.

RNA is required for SFPQ-RNA binding to KIF5A/KLC1

To identify the structural basis for the specificity in binding of SFPQ to the KIF5A/KLC1 motors, we first asked whether the C-terminal tail regions of KLC1 and KIF5A are required for SFPQ binding, as these regions are among the most variable compared with KLC2 and with KIF5B/C, respectively (Carpentier et al., 2015; Kanai et al., 2000). When we overexpressed either Myc-tagged WT KLC1 or its C-terminal mutant (ΔTail) in human embryonic kidney (HEK) 293T cells and assessed binding to SFPQ with coprecipitation studies, we found that binding is reduced by ∼50% in the absence of the C-terminal region of

KLC1 (Fig. 3, A–C). Similarly, we generated a tail-truncated mutant of KIF5A (ΔTail) that still retains the region responsible for KLC binding (Fig. 3, D and E; Diefenbach et al., 1998). Truncation of the tail region for KIF5A dramatically reduced the binding of SFPQ compared with KLC1 (Fig. 3, D, F, and G), while the tail region of KIF5A alone was able to bind to SFPQ (Fig. 3 D, F, and G). Together, these data demonstrate that SFPQ binding to KIF5A/KLC1 is enabled by the highly divergent C-terminal regions of both KLC1 and KIF5A and may explain the specificity of these interactions.

As RNA is a critical component of RNP granules, we asked whether the SFPQ that binds to KIF5A/KLC1 is also associated with RNA cargos. We expressed HA-SFPQ, FLAG (DYKDDDDK-tag)-KIF5A, and KLC1-Myc in HEK 293T cells and treated cell lysates with RNase or vehicle control. We then immunoprecipitated HA-SFPQ. Strikingly, we found that RNase treatment impeded the interaction between SFPQ and KIF5A-KLC1 (Fig. 3, H and I), demonstrating that KIF5A/KLC1 binds SFPQ only when it is associated with RNA. These findings suggest that KIF5A/KLC1 bind and transport SFPQ when it is part of a large RNP granule.

Binding of SFPQ to KIF5A/KLC1 by the Y-acidic motif is required for anterograde transport

KLCs bind to W- and Y-acidic motifs present within the cargo proteins. Cargos with the W-acidic motif bind to KLC1 and KLC2; however, such cargos as JIP1, which contains a Y-acidic motif, are selective for binding to KLC1 and not to KLC2 (Fig. S3 A; Nguyen et al., 2018; Pernigo et al., 2018). Interestingly, SFPQ does not have a W-acidic motif but does contain a Y-acidic motif within the coiled-coil domain. This motif is evolutionarily conserved and closely matches the Y-acidic sequence of JIP1 (Fig. 4 A). Mutation of the critical tyrosine within the Y-acidic motif of JIP1, JIP1^{Y709A} (Fig. S3 A), disrupts binding to KLC1 (Nguyen et al., 2018; Pernigo et al., 2018; Verhey et al., 2001). Therefore, we tested whether SFPQ binds in a similar fashion to KLC1 by similarly mutating the critical Y527 residue within the putative Y-acidic motif of SFPQ (SFPQ^{Y527A}). We purified human KLC1 and used isothermal titration calorimetry (ITC) to test binding by a SFPQ peptide that spans the Y-acidic motif. Intriguingly, WT SFPQ peptide binds to KLC1 with a dissociation constant (K_d) of 3.8 ± 2.3 µM, whereas the SFPQ^{Y527A} peptide did not bind to KLC1 in ITC assays (Fig. 4 B and Table 1). The K_d of the SFPQ peptide with KLC1 fragment is similar to that of previously reported JIP1 studies (Nguyen et al., 2018; Zhu et al., 2012; Pernigo et al., 2018), with binding affinity in the low micromolar range (Table 2).

Previous studies identified sequences within KLC1 that are not present in KLC2 and that specify binding to the Y-acidic motif within JIP1. One key residue in KLC1 is N343 within the TPR4 region of KLC1 (Fig. S3 B). Mutation of this residue to a serine, as observed in KLC2, abrogates the interaction between JIP1 and KLC1 (Zhu et al., 2012). To determine whether N343 on KLC1 mediates binding to SFPQ, we expressed Myc-tagged WT or KLC1^{N343S} together with HA-tagged SFPQ in HEK 293T cells. Surprisingly, KLC1^{N343S} did not alter binding to SFPQ, in contrast to JIP1 (Fig. S3 C). These data suggest that the specificity of binding of JIP1 and SFPQ to KLC1 both require the Y-acidic motif; however, the mode of interaction may be distinct at the structural level.

ITC binding studies assess interactions between a peptide sequence of SFPQ that is 17 amino acids in length and a purified KLC1 protein. We next tested whether the Y-acidic motif is required for SFPQ binding to the KIF5A/KLC1 motor in a complex cellular milieu. Similar to the results observed with ITC, the SFPQ^{Y527A} mutation drastically reduces binding between SFPQ and KIF5A/KLC1. Together, these data demonstrate that the Y-acidic motif within SFPQ is required for binding to the KIF5A/KLC1 motor complex (Fig. 4, C and D).

To determine whether binding of SFPQ to KIF5A/KLC1 motors is required for anterograde transport of SPFQ in axons, we expressed a Halo-tagged WT SFPQ (Video 1) or SFPQ^{Y527A} mutant (Video 2) in DRG neurons that were grown in microfluidic chambers (Fig. 4 E). In SFPQ^{Y527A}-expressing neurons (Video 2), the number of SFPQ particles localized to distal axons was reduced by ∼50% (Fig. 4 F), while SFPQ^{Y527A} accumulated in the CB to a greater extent than did WT protein (Fig. S4 A). Moreover, of SFPQ particles that reached the axons, SFPQ^{Y527A} mutant exhibited an ∼50% reduction in the percentage of time spent in anterograde axonal transport compared with WT SFPQ (Fig. 4 G). Since SFPQ forms a dimer, residual movement of SFPQ^{Y527A} may reflect binding of KIF5A/KLC1 motors to dimeric SFPQ that contains both endogenous WT SFPQ and the fluorescent mutant isoform (Hewage et al., 2019). Reduction in the percentage of time spent in anterograde transport resulted in a concomitant increase in the percentage of time spent in retrograde transport by SFPQ^{Y527A} (Fig. S5 B). Average anterograde/retrograde run length and average anterograde velocity were the same in WT and SFPQ^{Y527A}, while average retrograde velocity actually increased in SFPQ^{Y527A} (Fig. S5, C and D).

To determine whether SFPQ^{Y527A} retains liquid-like properties, we analyzed the shape aspect ratio of SFPQ^{Y527A} as it moves through the axons (Fig. S4 E). Like WT SFPQ, the shape aspect ratio for SFPQ^{Y527A} increased during both anterograde and retrograde movement, and there were no differences identified due to this mutation (Fig. S4 F). Together, these data demonstrate that binding of SFPQ to the KIF5A/KLC1 motor complex is required for axonal localization and anterograde transport within sensory axons, and is not involved in determining the liquid phase properties of these RNA-RBP granules.

Defect in KIF5A/KLC1-driven transport of SFPQ leads to axon degeneration in DRG sensory neurons

To determine the physiologic consequences of impeding SFPQ transport by KIF5A/KLC1, we leveraged SFPQ^{Y527A}-expressing neurons. As shown previously, knockdown of SFPQ results in axon degeneration (Fig. 5, A and B; Cosker et al., 2016). The degree of degeneration was quantified by analyzing the ratio of the area of the fragmented axons over the total axon area, referred to as degeneration index (Sasaki et al., 2009). We then assessed the ability of constructs encoding either WT SFPQ or SFPQ^{Y527A} to reverse the degeneration caused by knockdown of SFPQ using constructs resistant to shRNA (Fig. 5 C). Interestingly, although WT SFPQ rescued degeneration and returned the degeneration index to baseline levels seen in control cultures,

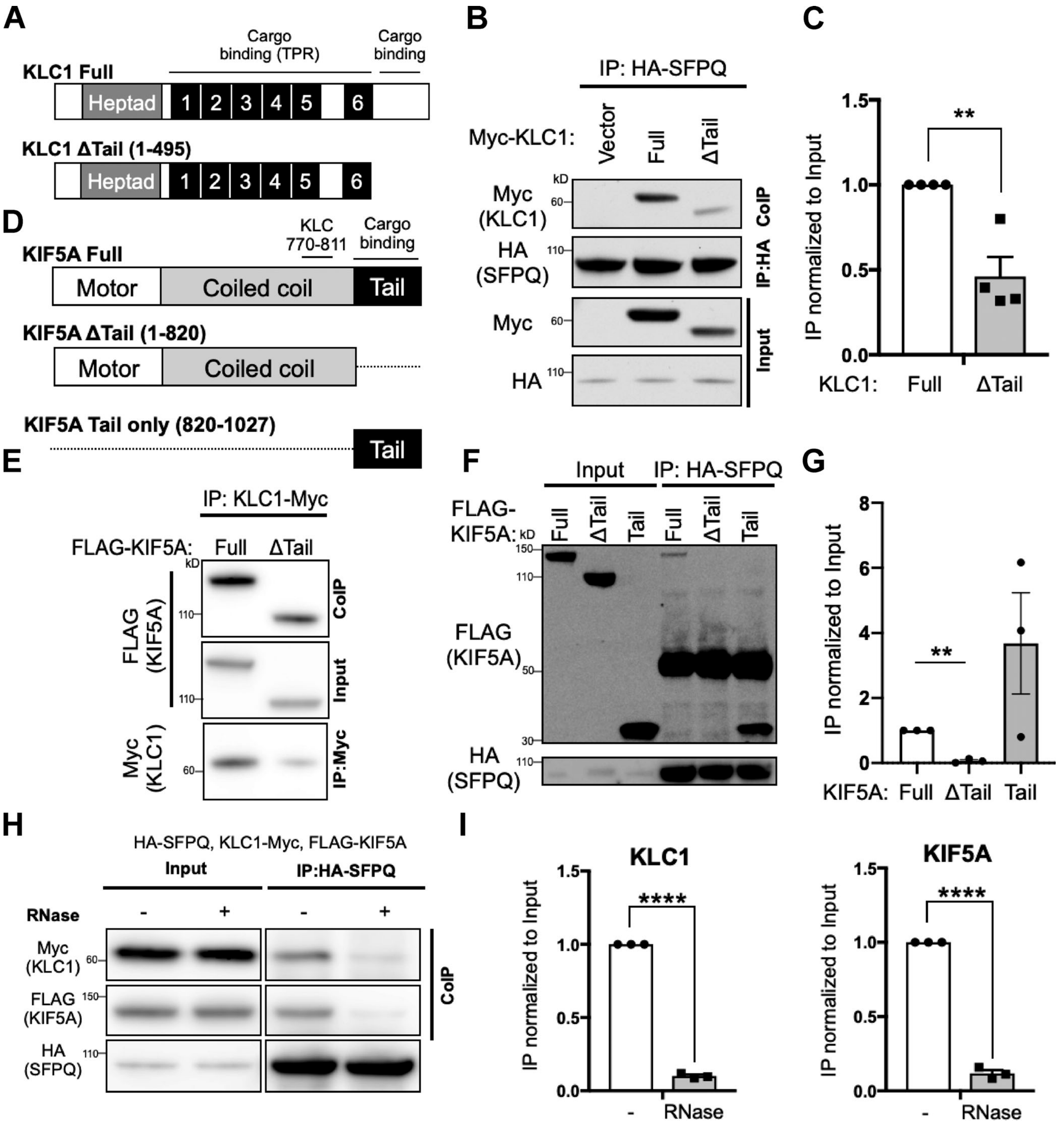

Figure 3. **RNA is required for SFPQ-RNA binding to KIF5A/KLC1. (A)** Schematic of the indicated constructs for KLC1. **(B)** HEK 293T cells transfected with HA-SFPQ with empty vector, full-length WT, or tail-truncated Myc-KLC1. HA was immunoprecipitated and blotted for Myc and HA. **(C)** Quantification of pull down in B relative to input. $^{**}P = 0.0033$ by unpaired two-tailed *t* test; $n = 4$; data represent mean ± SEM. **(D)** Schematic of the indicated constructs for KIF5A. KLC binding region is indicated. **(E)** HEK 293T cells transfected with KLC1-Myc and with either WT FLAG-tagged KIF5A or the ΔTail mutant. Myc was immunoprecipitated and blotted for FLAG and Myc. **(F)** HEK 293T cells transfected with HA-SFPQ with full-length WT, tail-truncated, or tail only FLAG-tagged KIF5A. HA was immunoprecipitated and blotted for FLAG and HA. **(G)** Quantification of pull down in F relative to input; $^{**}P = 0.0014$ by independent Welch's *t* test; $n = 3$; data represent mean ± SEM. **(H)** HEK 293T cells transfected with HA-SFPQ, KLC1-Myc, and FLAG-KIF5A, and lysates were treated with or without RNase. HA was immunoprecipitated and blotted for HA, Myc, and FLAG. **(I)** Quantification of pull down of KLC1-Myc or FLAG-KIF5A (bottom) in H relative to input; $^{****}P < 0.0001$ by unpaired two-tailed *t* test; $n = 3$; data represent mean ± SEM. For B, E, F, and H, input represents 0.5% of 0.5 mg of protein lysate used for IP. Total eluate from the bead was run on the gel. Heptad, Heptad repeat; TPR, tetratricopeptide repeat.

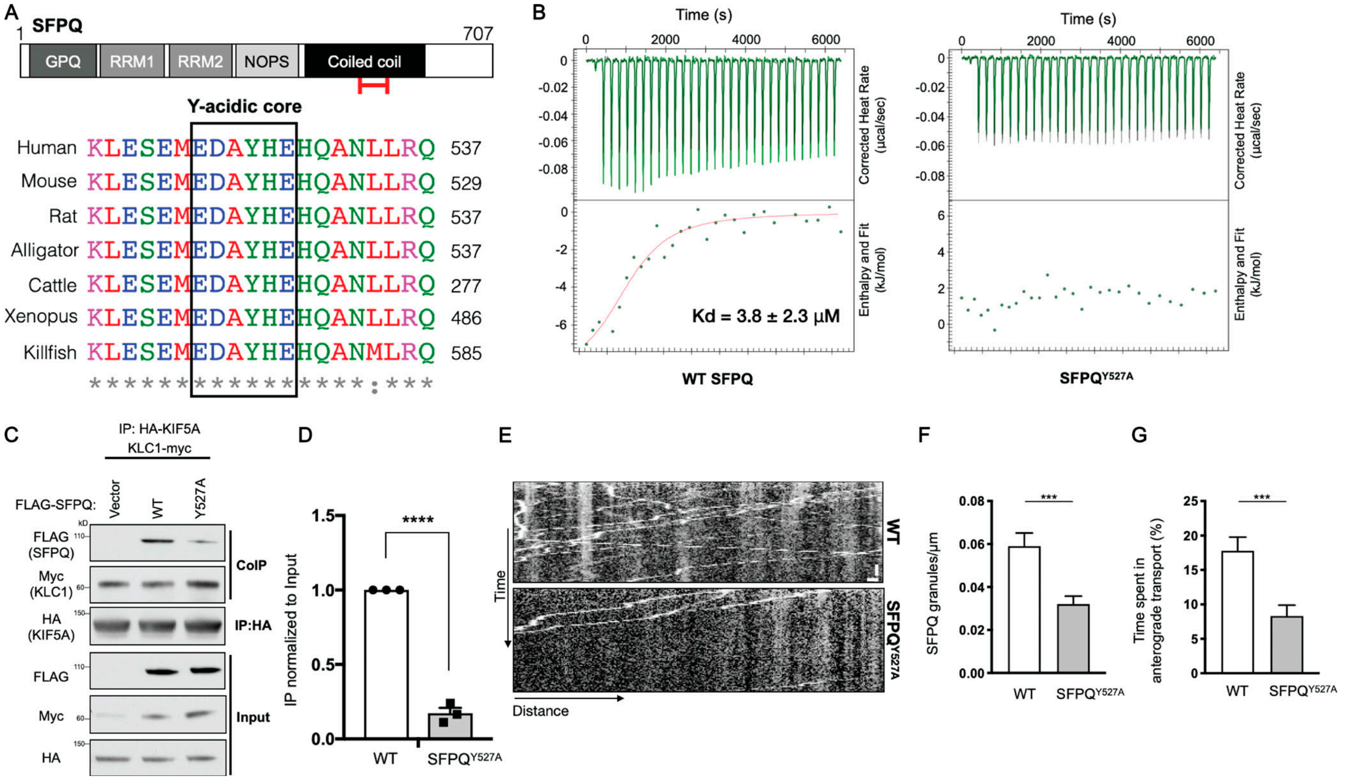

Figure 4. **Binding of SFPQ to KIF5A/KLC1 by the Y-acidic motif is required for anterograde transport. (A)** Alignment of the sequence within the coiled-coil domain of SFPQ containing the Y-acidic motif. Bottom: Schematic of the domains of SFPQ; red bracket indicates the region containing the Y-acidic motif. **(B)** ITC measurements of the reference KLC1 (TPR1-6) fragment with either the WT SFPQ peptide (ESEMEDAYHEHQANLLR) or the SFPQ^{Y527A} peptide (ESEMEDAAHEHQANLLR). **(C)** HEK 293T cells transfected with HA-KIF5A, KLC1-Myc, and with either empty vector, full-length FLAG-tagged WT SFPQ, or SFPQ^{Y527A}. HA was immunoprecipitated and blotted for FLAG, Myc, and HA. Input represents 0.5% of 0.5 mg of protein lysate used for SFPQ IP, and total elute from the bead was run on the gel. **(D)** Quantification of pull down in C relative to input; ****P < 0.0001 by unpaired two-tailed *t* test; *n* = 3; data represent mean ± SEM. **(E)** Kymograph of Halo-tagged WT SFPQ and SFPQ^{Y527A} in axons of DRG neurons. Scale Bars: 2 µm and 15 s. **(F)** Average number of Halo-tagged WT SFPQ and SFPQ^{Y527A} granules per micron of axon length. Data from WT SFPQ control (*n* = 31) and SFPQ^{Y527A} (*n* = 34) axons analyzed across at least four independent microfluidic experiments. ***P = 0.0003 by unpaired two-tailed *t* test; data represent mean ± SEM. **(G)** Average percentage of time spent in anterograde transport for Halo-tagged WT SFPQ and SFPQ^{Y527A} in axons of DRG sensory neurons. Data represents 258 granules for WT SFPQ control and 202 granules for SFPQ^{Y527A} analyzed from at least 30 axons across at least four independent microfluidic experiments. ***P = 0.0004 by unpaired two-tailed *t* test; data represent mean ± SEM. GPQ, glycine proline glutamine-rich; NOPS, NONA/paraspeckle domain; RRM, RNA recognition motif.

expression of SFPQ^{Y527A} did not prevent degeneration and resulted in a level of degeneration that was similar to that observed in the absence of SFPQ (Fig. 5 B). Taken together, these data indicate that transport of SFPQ is required for axon survival and demonstrate that defects in KIF5A/KLC1-driven transport of SFPQ causes degeneration of sensory axons.

CMT2-associated *KIF5A^{R280H}* disrupts SFPQ binding and alters localization of its mRNA cargo

Our data indicate that KIF5A/KLC1 functions to transport SFPQ-RNA granules within DRG sensory neurons, and that this transport process is required for axon survival (Fig. 6 A). Thus, transport of SFPQ by KIF5A/KLC1 motors may be a key pathway disrupted by *KIF5A* mutations in CMT2. Two independent studies have reported a mutation *KIF5A^{R280H}* that results in a pure classical form of CMT2 (Fig. 6 B; Liu et al., 2014; Nam et al., 2018). Both structural and biochemical characterizations indicate that KIF5A^{R280H} exhibits reduced microtubule binding affinity and decreased motility compared with WT KIF5A (Dutta et al., 2018; Ebbing et al., 2008; Füger et al., 2012; Jennings et al., 2017). Interestingly, although the mutation resides within the motor domain, KIF5A^{R280H} exhibited an ~50% reduction in binding to SFPQ compared with WT KIF5A (Fig. 6 C). Therefore, this pathologic mutation in KIF5A may disproportionately affect transport of the SFPQ-containing RNA cargo due to altered binding to SFPQ as well as reduced motility.

Table 1. **ITC parameters between KLC1 TPR1-6 fragment and WT or SFPQ^{Y527A} peptide**

SFPQ (syringe)	*n*	K_d (µM)	ΔH (kj/mol)	ΔS (J/mol•K)
WT	0.964 ± 0.143	3.833 ± 2.310	-8.580 ± 1.834	74.92
Y527A	No binding			

Table 2. **K_d comparison of SFPQ and JIP1 with KLC1**

Protein and peptide	Region	K_d (µM)
KLC1 TPR1-6 (our study)	KLC1: 205-501	3.833 ± 2.310
SFPQ	SFPQ: ESEMEDAYHEHQANLLR	
KLC1 TPR1-6 (Zhu et al., 2012)	KLC1: 228-495	9.4 ± 5.85
JIP1	JIP1: EYTCPTEDIYLE	
KLC1 TPR1-6 (Nguyen et al., 2018)	KLC1: 205-502	5.0 ± 0.5
JIP1	JIP1: TCPTEDIYLE	
KLC1 TPR1-6 (Pernigo et al., 2018)	KLC1: 205-496	11.66 ± 1.85
JIP1	JIP1: YTCPTEDIYLE	

To model axon degeneration induced by *KIF5A*^{R280H} in vitro, we expressed KIF5A^{R280H} by lentivirus in DRG sensory neurons that also express the endogenous WT KIF5A. As observed in patients who were heterozygous for CMT2 mutations (Liu et al., 2014; Nam et al., 2018), overexpression of KIF5A^{R280H} led to axon degeneration in DRG sensory neurons (Fig. 6, D and E), while overexpression of WT does not compromise axon integrity (Fig. 6, D and E). As KIF5A^{R280H} exhibits reduced binding to

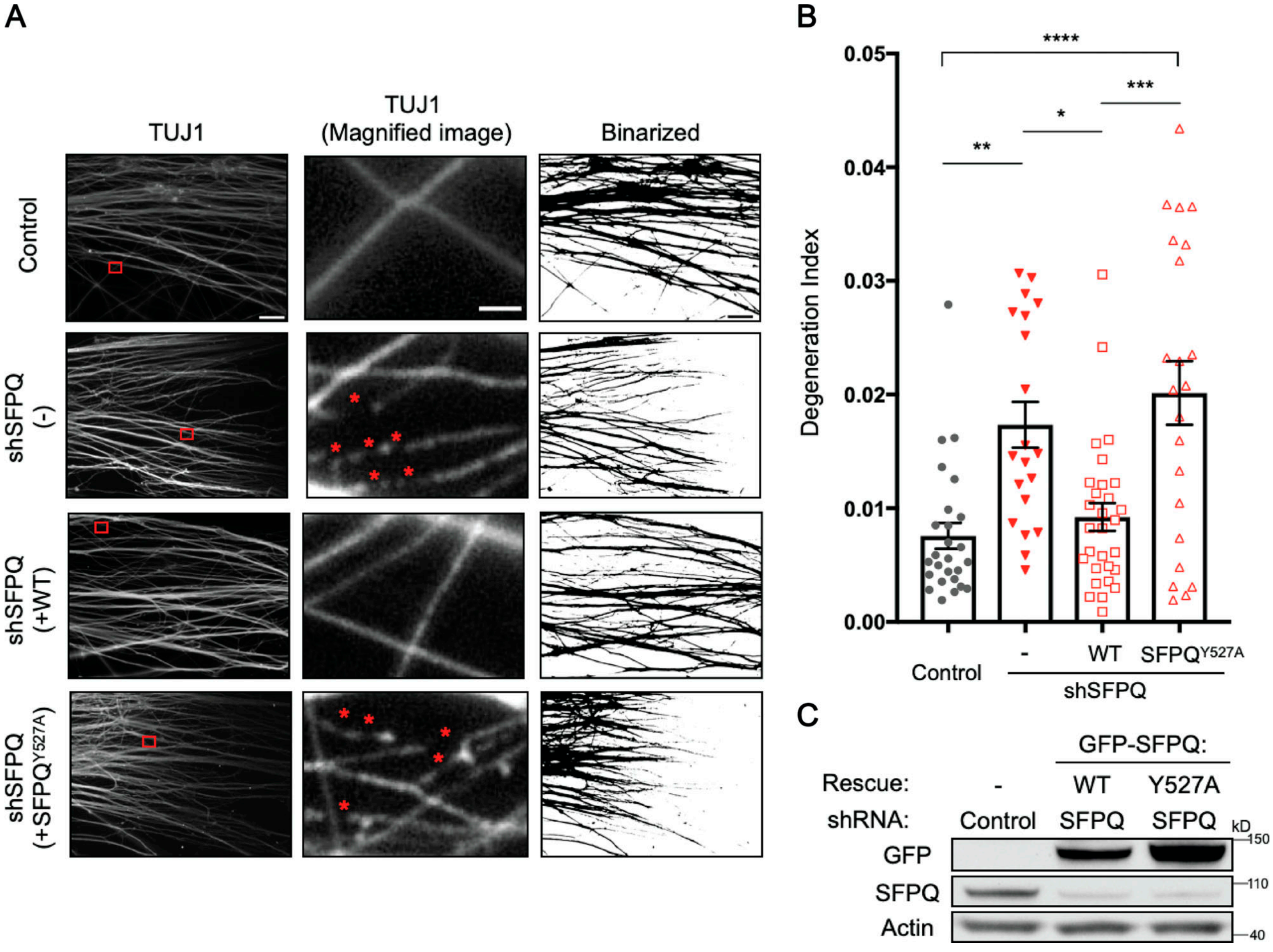

Figure 5. **Defect in KIF5A/KLC1-driven transport of SFPQ leads to axon degeneration in DRG sensory neurons. (A)** Examples of TUJ1 immunostaining. Magnified view depicts individual axon morphology, and corresponding binarized images show axons of DRG neurons grown in compartmented cultures expressing control or shSFPQ rescued with empty vector (-), WT SFPQ, or SFPQ^{Y527A}. Red boxes outline regions shown for the higher magnification view of axons. Asterisks indicate interruptions in TUJ1 continuity. Scale bar: 100 µm and 10 µm (magnified image). **(B)** Quantification of axonal degeneration from A, which is calculated by using the ratio of the region of fragmented axons to total axon area (degeneration index [Sasaki et al., 2009]). Control (*n* = 26 captured images) or shSFPQ rescued with empty vector (*n* = 20), WT SFPQ (*n* = 29), or SFPQ^{Y527A} (*n* = 22). *P = 0.0112; **P = 0.0019; ***P = 0.0002; ****P < 0.0001 by one-way ANOVA; data from 3 independent experiments; data represent mean ± SEM. **(C)** DRG neurons were infected with control or shRNA against SFPQ and rescued with empty, GFP-tagged WT, or SFPQ^{Y527A}. Protein lysates were blotted against GFP, endogenous SFPQ, and actin as loading control.

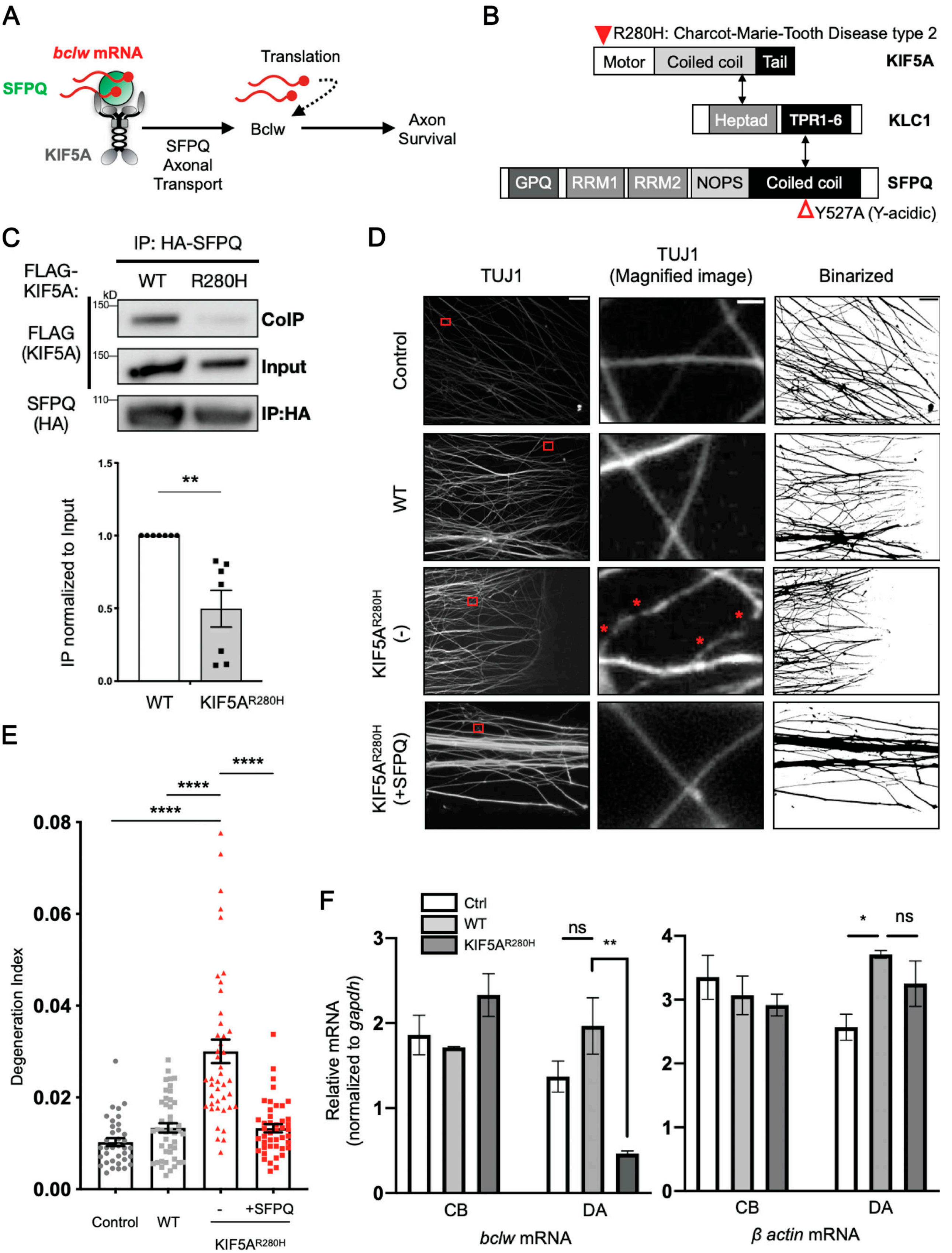

Figure 6. **CMT2-associated *KIF5A*^{R280H} disrupts SFPQ binding and alters localization of its mRNA cargo. (A)** A schematic model for axon survival mediated by preferential transport of SFPQ by the KIF5A motor. bclw is an mRNA bound to SFPQ and its local translation in axons mediates axon survival (Cosker et al., 2016; Cosker et al., 2013). **(B)** A schematic representation of KIF5A, KLC1, and SFPQ. Red closed arrowhead indicates the location of KIF5A^{R280H}

CMT2 mutation, and open arrowhead indicates the location of $SFPQ^{Y527A}$ (Y-acidic motif). **(C)** Top: HEK 293T cells transfected with HA-SFPQ, and with either FLAG-tagged WT KIF5A or $KIF5A^{R280H}$. HA was immunoprecipitated and blotted against FLAG and HA. Input represents 0.5% of 0.5 mg of protein lysate used for HA IP; total elute from the bead was run on the gel. Bottom: Quantification of precipitated protein normalized to input. $^{**}P = 0.0019$ by unpaired two-tailed *t* test; $n = 7$; data represent mean ± SEM, **(D)** Examples of TUJ1 immunostaining. Magnified view depicts individual axon morphology, and corresponding binarized images show axons of DRG neurons grown in compartmented cultures expressing control, WT KIF5A, $KIF5A^{R280H}$, and $KIF5A^{R280H}$ rescued with SFPQ. Red boxes outline regions shown for the higher magnification view of axons. Asterisks indicate interruptions in TUJ1 continuity. Scale bar: 100 µm and 10 µm (magnified image). **(E)** Quantification of axonal degeneration from E, which is calculated by using the ratio of the region of fragmented axons to total axon area (degeneration index [Sasaki et al., 2009]). Control ($n = 36$ captured images), WT KIF5A ($n = 44$), $KIF5A^{R280H}$ ($n = 43$), or $KIF5A^{R280H}$ + SFPQ ($n = 44$) from three independent experiments; $^{****}P < 0.0001$ by one-way ANOVA; data represent mean ± SEM. **(F)** *bclw* and *β actin* mRNA quantified by quantitative RT-PCR from CB and distal axons (DA) from compartmented cultures for control (Ctrl), WT KIF5A, $KIF5A^{R280H}$-expressing neurons. Data normalized to *gapdh*; $^{**}P = 0.0068$; $^{*}P = 0.0342$ by one-way ANOVA; data from three independent experiments; data represent mean ± SEM.

SFPQ compared with WT KIF5A, we next tested whether SFPQ overexpression prevents this axon degeneration. Intriguingly, overexpression of SFPQ rescued axon degeneration caused by $KIF5A^{R280H}$ CMT2 mutation (Fig. 6, D and E).

To gain mechanistic insight into the changes in transport caused by $KIF5A^{R280H}$, we tested the effects of the mutant KIF5 on axonal mRNAs. Axonal levels of *bclw* mRNA, an mRNA cargo of SFPQ (Cosker et al., 2016), are significantly decreased in neurons expressing $KIF5A^{R280H}$ compared with WT control, whereas axonal expression of *β actin* mRNA, which is not bound by SFPQ (Cosker et al., 2016), was not affected (Fig. 6 F). We further tested whether the defect is specific to SFPQ cargo by directly visualizing mitochondria, which are transported by KIF5A (Campbell et al., 2014). Intriguingly, in DRG sensory neurons, $KIF5A^{R280H}$ did not alter mitochondria transport or the percentage of time spent in stationary, anterograde, or retrograde transport; anterograde/retrograde run length and velocity were not statistically different between control and $KIF5A^{R280H}$ (Fig. S5, A–D). Together, these data demonstrate that $KIF5A^{R280H}$ exhibits reduced binding to SFPQ and impacts the axonal localization of mRNA cargoes of SFPQ.

Axon degeneration due to CMT2-associated *KIF5A*^{R280H} mutation rescued by a Bclw mimetic peptide

KIF5A motors are involved in transport of mitochondria, vesicles, and RNA granules; therefore, degeneration of axons caused by *KIF5A*^{R280H} could be a consequence of defect in the transport of any or all of these cargos. A similar pattern of axon degeneration is observed in sensory neurons expressing $SFPQ^{Y527A}$, suggesting that SFPQ-RNA granules may represent a critical cargo among the many impacted in CMT2 patients with *KIF5A*^{R280H}. Local translation of mRNAs bound to SFPQ is a critical step that promotes axon survival (Cioni et al., 2019; Cosker et al., 2016). *bclw* is one such mRNA that is bound by SFPQ and translated in axons of DRG sensory neurons (Fig. 6 A; Cosker et al., 2016). Our data indicate that axonal levels of *bclw* are reduced by *KIF5A*^{R280H} mutation. To determine whether axon degeneration can be rescued by restoring Bclw activity in axons, we introduced into axons a stabilized α-helix of the Bcl2 domain modeled after the Bclw BH4 sequence (called Bclw BH4 $SAHB_A$). As a control, we instead introduced into axons a closely related BH4 $SAHB_A$ modeled after the Bcl2 sequence (Fig. 7, A and B; Barclay et al., 2015; Pease-Raissi et al., 2017). Intriguingly, the BH4 peptide mimetic of Bclw introduced into axons of $KIF5A^{R280H}$-expressing neurons prevents axon degeneration in this genetic model of CMT2 (Fig. 7, C and D). This effect is specific to Bclw, since introducing a Bcl2 mimetic peptide did not prevent degeneration, and degeneration remained at the level observed with $KIF5A^{R280H}$-expressing neurons (Fig. 7, C and D). Taken together, these data suggest that defective transport of SFPQ-RNA granules containing *bclw* mRNA represents one of the key mechanisms that causes neurodegeneration in CMT2 and may be a robust targetable pathway for therapeutic intervention.

Discussion

Kinesins are a large family of microtubule-dependent motors that play a pivotal role in intracellular transport of multiple organelles. These motors are particularly critical in neurons, which establish extensive axonal and dendritic projections and so rely on fast transport across long distances. While mutations that affect kinesin motors cause diverse neurodegenerative diseases, it is not known whether this reflects a requirement for specific kinesins in mediating the transport of particular cargos within the lengthy axons that extend to peripheral targets, or whether degeneration reflects a more global loss of axonal transport. Here, we show that SFPQ-containing transport granules preferentially interact with kinesin containing the KIF5A heavy chain and the cargo adaptor KLC1. Therefore, mutations in *KIF5A* that cause sensory neuropathy preferentially impact motility of SFPQ granules that transport *bclw* and other mRNAs, and the degeneration caused by *KIF5A* mutations can be prevented by a peptide that mimics the function of the locally translated protein Bclw.

There are more than 40 genes that encode kinesins, 38 of which are expressed in the nervous system (Miki et al., 2001). Conventional kinesin-1 motor was the first member of the family identified (Brady, 1985; Vale et al., 1985). In humans and in other mammals, kinesin-1 is encoded by three distinct *KIF5* genes, *KIF5A*, *KIF5B*, and *KIF5C*. These three genes are ∼75% identical and were initially thought to be functionally redundant; however, the KIF5 motors are differentially expressed. KIF5B is ubiquitous while KIF5A and KIF5C are expressed predominantly in the nervous system (Kanai et al., 2000). Within neurons, KIF5 motors are particularly critical for axonal transport (Huang and Banker, 2012; Jacobson et al., 2006; Lipka et al., 2016; Nakata and Hirokawa, 2003; Tas et al., 2017). Here, we show that in DRG sensory neurons, KIF5B is predominantly located in the cell soma, while KIF5A and KIF5C are found in the

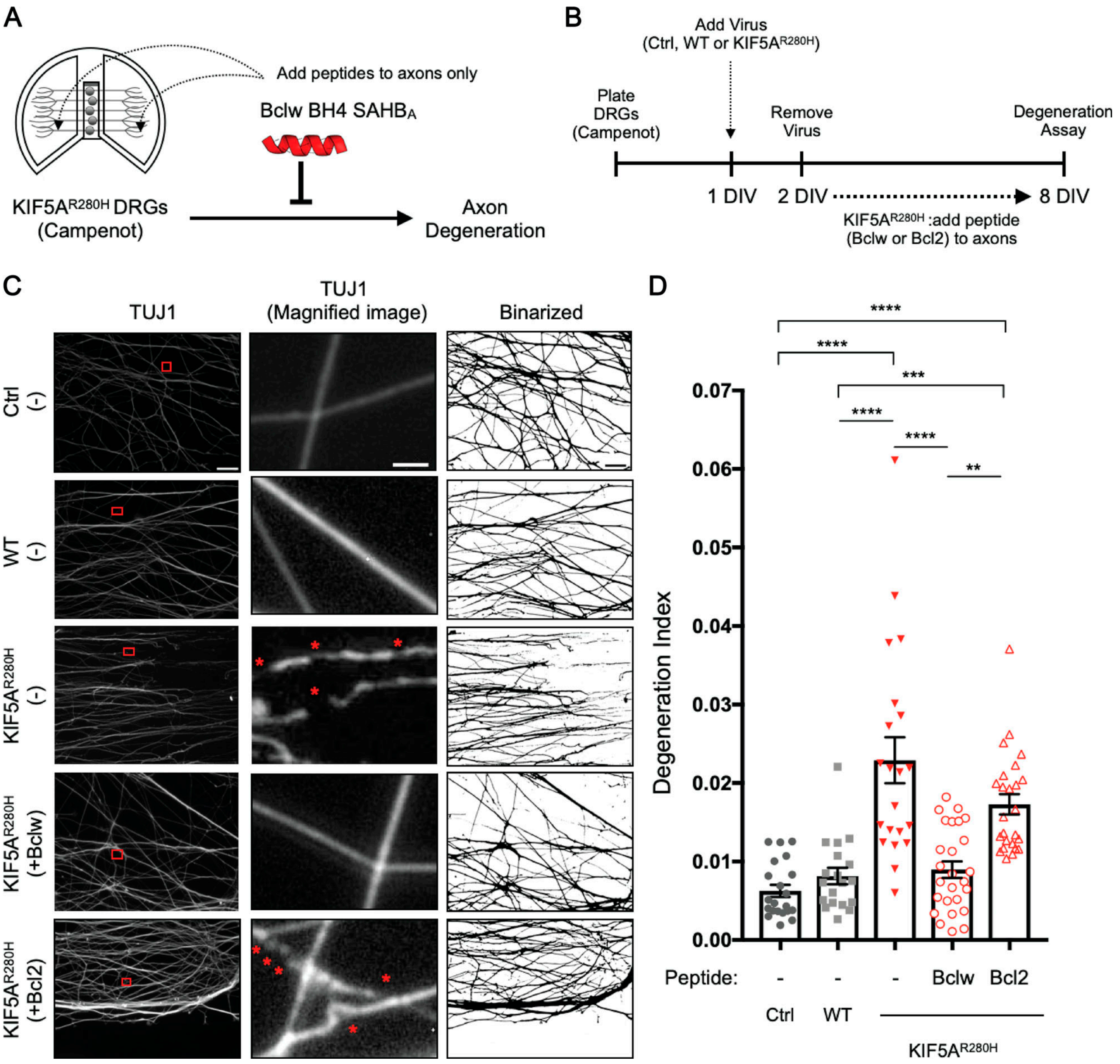

Figure 7. **Axon degeneration due to CMT2-associated *KIF5A^{R280H}* mutation rescued by a Bclw mimetic peptide. (A)** Schematic representation of a Bclw peptide mimetic rescue experiment. A stabilized α-helix of Bcl2 domain of Bclw (called Bclw BH4 SAHB$_A$; 20 amino acid) was introduced into axons of DRG neurons grown in Campenot cultures. **(B)** Experimental design of the Bclw mimetic peptide rescue experiment in DRG neurons cultured in compartmented Campenot chambers. **(C)** Examples of TUJ1 immunostaining; magnified view depicting individual axon morphology; and corresponding binarized images of axons of DRG neurons grown in compartmented cultures expressing control, WT KIF5A, or KIF5A^{R280H} with either no peptide, Bclw, or Bcl2 peptide. Red boxes outline regions shown for the higher magnification view of axons. Asterisks indicate interruptions in TUJ1 continuity. Scale bar: 100 µm and 10 µm (magnified image). **(D)** Quantification of axonal degeneration from C, which is calculated by using the ratio of the region of fragmented axons to total axon area (degeneration index [Sasaki et al., 2009]). Control (Ctrl; *n* = 21 captured images), WT KIF5A (*n* = 19), KIF5A^{R280H} with either no peptide (*n* = 21), Bclw (*n* = 26), or Bcl2 peptide (*n* = 25). From three independent experiments; $^{**}P = 0.0011$; $^{***}P = 0.0010$; $^{****}P < 0.0001$ by one-way ANOVA; data represent mean ± SEM.

long axons of these neurons (Fig. 2 H and Fig. S2, F and G). Moreover, we demonstrate that the distinct KIF5 proteins exhibit selectivity for cargo binding, as the RBP SFPQ preferentially associates with and is transported by KIF5A motors.

The C-terminal domain is the region of KIF5 isoforms that exhibits the greatest variability. This region has previously been implicated in cargo binding (Campbell et al., 2014; Randall et al., 2013; Setou et al., 2002; Xu et al., 2010; Zhao et al., 2020), and we find that this distinctive KIF5A C-terminal region is required for binding to SFPQ (Fig. 3, F and G). KLC1 is the selective KLC that associates with KIF5A to bind and transport SFPQ (Fig. 2 F and Fig. 3, A–C). Intriguingly, the KLC1 isoform that coimmunoprecipitates with SFPQ in DRG neurons exhibits a higher apparent molecular weight than total KLC1, and this mobility shift reflects changes in phosphorylation state (Fig. 2 F and Fig. S2 D). Neurotrophin stimulation leads to decreased KLC1 phosphorylation (Fig. S2 E), which may enable the release of SFPQ-RNA granules from kinesin motors. We hypothesize that low neurotrophin levels at the CB enables phosphorylation of KLC1 and enhances the binding of SFPQ-RNA granules to active kinesin motors. In axon terminals, signaling by target-derived neurotrophins alters the phosphorylation state of KLC1 and interrupts the binding of SFPQ-RNA granules to motor proteins and so allows for release and local translation of the mRNA. Interestingly, a similar regulatory mechanism has been proposed for Fragile X mental retardation protein (FMRP)/miR-181d granules, as neurotrophin stimulation causes release of *Map1b* and *Calm1* mRNA (Wang et al., 2015).

We have identified a critical motif in SFPQ that enables binding to distinctive KIF5A/KLC1 motors. SFPQ contains a Y-acidic motif (Nguyen et al., 2018; Pernigo et al., 2018) that closely resembles the previously characterized Y-acidic motifs in JIP1, TorsinA, and SH2D6 that enable selective binding to motors containing KLC1 rather than KLC2. While the previously identified Y-acidic motifs are found within unstructured regions (Nguyen et al., 2018; Pernigo et al., 2018), the motif within SFPQ resides in the highly structured coiled-coil region (Fig. 4 A). In accordance with this difference, KLC1^{N343S}, which disrupts interaction with JIP1 (Zhu et al., 2012; Pernigo et al., 2018), has no effect on binding with SFPQ (Fig. S3 C). A further distinction is the nature of the transported organelles: JIP1 is associated with membrane bound organelles, whereas SFPQ is part of an RNP granule.

SFPQ-containing RNA granules display properties that are typical of nonmembrane enclosed organelles. SFPQ contains an intrinsically disordered region in its N-terminal region (Fig. S1 A) and is assembled into large RNA transport granules, which are usually viewed as nonmembrane enclosed organelles (Kanai et al., 2004). Live cell imaging indicates that SFPQ particles within axons display liquid-like properties as they are deformed by fast transport (Fig. 1, A and B). Similarly, nuclear SFPQ and other members of the *Drosophila* behavior/human splicing proteins, NONO and PSPC1, form the core components of paraspeckle nuclear bodies, a well-recognized phase-separating structure (Hirose et al., 2019). It was recently shown that RNA fragments of NEAT1_2 bind SFPQ to induce higher-order assembly needed for paraspeckle formation (Yamazaki et al., 2018). As is the case for paraspeckle formation, RNA is a critical component of transport granules and promotes the interaction between SFPQ and kinesin motors; RNase treatment leads to the loss of integrity of these axonal granules (Knowles et al., 1996) and prevents binding between SFPQ and KIF5A/KLC1 (Fig. 3, H and I). Thus, binding to mRNA cargos, such as *bclw*, may induce a conformational change in SFPQ that facilitates oligomerization and phase separation and that exposes the Y-acidic motif for KLC1 binding. Detailed structural studies addressing the mechanism whereby specific RNA cargos alter the conformation and/or phase separation of SFPQ will be necessary to fully evaluate this hypothesis.

In this study, we show that the pathway involving transport of SFPQ by KIF5A/KLC1 is a robust and targetable contributor to CMT2, as demonstrated by the ability of a Bclw peptide mimetic to rescue axon degeneration caused by *KIF5A*^{R280H} (Fig. 7, C and D). Our data demonstrate a reduced level of axonal *bclw* mRNA in neurons expressing KIF5A^{R280H} (Fig. 6 F) and indicate that transport of *β actin* (Fig. 6 F) and mitochondria (Fig. S5) are not affected. Although additional KIF5A cargo may also be impacted by KIF5A^{R280H}, our findings suggest that Bclw peptide mimetics replenish axonal Bclw proteins levels and are sufficient to prevent axon degeneration in the setting of CMT2-associated KIF5A mutations. Mutations in *Rab7a* that cause CMT2B (Cioni et al., 2019) also alter axonal translation of mRNAs bound by SFPQ (Cioni et al., 2019) and suggest that other peripheral neuropathies may also be responsive to Bclw mimetics.

SFPQ-RNA granules are critical for development and maintenance of axons in motor neurons and sensory neurons, and human mutations in *SFPQ* and in *KIF5A* have been implicated in ALS (Thomas-Jinu et al., 2017). Interestingly, the SFPQ^{Y527A} residue of the Y-acidic motif lies adjacent to the two identified ALS mutations, N533H and L534I. These two mutations lead to a loss of the axonal pool of SFPQ in motor neurons (Thomas-Jinu et al., 2017), and our data suggest that this may be through altered binding of SFPQ to KIF5A/KLC1. Moreover, ALS-associated mutations in *KIF5A* lead to the incorporation of a new protein sequence in the C-terminal region of the protein (Nicolas et al., 2018), the domain that is required for SFPQ binding. Therefore, altered binding and axonal transport of SFPQ may also be a mechanism underlying axon degeneration of motor neurons in patients harboring ALS-associated mutations in *SFPQ* or *KIF5A*. Disrupted axonal function of SFPQ may also be implicated in axonal degenerative diseases that do not exhibit mutations in *SFPQ* or *KIF5A*—for instance, a recent study demonstrated that aberrant localization of SFPQ is a molecular hallmark of multiple familial and sporadic models of ALS (Luisier et al., 2018). As our study reveals the importance of studying endogenous levels of KIF5 motors in a physiologically relevant system, it will be critical to determine whether KIF5A also preferentially binds to SFPQ in other neuronal subtypes as well as to model ALS-causing mutations of *KIF5A* and *SFPQ* with human induced pluripotent stem cells (iPSC)-derived motor neurons. Together, our data suggest that Bclw mimetics may serve as a potential therapeutic intervention for preventing axon degeneration in neurologic diseases with defective RNA transport, including CMT and possibly ALS.

Materials and methods

All experimental procedures were done in accordance with the National Institutes of Health guidelines and were approved by the Dana-Farber Cancer Institutional Animal Care and Use Committee.

Please refer to Table S1 for a full list of reagents and resources used in this paper.

Animal use

Time pregnant Sprague-Dawley rats were purchased from Charles River.

DNA and shRNA constructs

Constructs used for HEK 293T immunoprecipitation (IP) studies were cloned into pcDNA3.1 vector by using PCR-based In-Fusion HD cloning (Clontech). KIF5 (pBa-GFP-lnkr-mmKIF5A;

pBa-GFP-mmKIF5B; pBa-mCherry-myc-KIF5C) and KLC1 (pBa-GFP-3myc-mmKLC1a) constructs were a gift from Dr. Gary Banker (Oregon Health and Science University, Portland, OR) and Dr. Marvin Bentley (Rensselaer Polytechnic Institute, Troy, NY) and were used as a template to PCR to clone the following HA-, FLAG-, or Myc-tagged constructs: HA-KIF5A, FLAG-KIF5A (WT, ΔTail, tail only, and R280H), KLC1-Myc (WT and N343S), and Myc-KLC1 (WT and ΔTail). The human version of SFPQ (hsSFPQ pcS2) was a gift from Dr. Corinne Houart (Kings's College London, London, UK) and was used to clone the following HA- and FLAG-tagged constructs: HA-SFPQ and FLAG-SFPQ (WT and Y527A). The $KIF5A^{R280H}$, $KLC1^{N343S}$, and $SFPQ^{Y527A}$ mutants were generated by using Q5 site-directed mutagenesis (New England Biolab) using manufacturer's instructions. Lentiviral constructs used for compartmented Campenot cultures were cloned into pLV-EF1a-IRES-Puro, a gift from Tobias Meyer (Stanford University, Stanford, CA; Addgene plasmid #85132), for KIF5A-HA (WT and R280H); pLV-EF1a-IRES-mCherry for GFP-SFPQ (WT and Y527A); and pLV-EF1a for Halo-SFPQ (WT). For live cell imaging of SFPQ, Halo-tagged SFPQ (WT and Y527A) was cloned into plasmid FUGW (flap-Ub promoter-GFP-WRE), a gift from David Baltimore (California Institute of Technology, Pasadena, CA; Addgene plasmid #14883), as a backbone vector. shRNAs against shSFPQ (TRCN0000102240), KIF5A (TRCN0000415243), and KIF5C (TRCN0000090857) were purchased from Sigma-Aldrich.

DRG sensory neuron culture

DRGs from embryonic day 15 rats of either sex were dissected and trypsinized. For mass cultures, 300,000 cells were plated onto p35 dishes coated with Corning Matrigel GFR Membrane Matrix (Thermo Fisher Scientific) diluted in DMEM (Thermo Fisher Scientific). Cultures were maintained in neurobasal (Invitrogen) with 2% B27 supplement (Invitrogen), 1% penicillin/streptomycin, 1% GlutaMAX (Life Technologies), and 0.08% glucose at 37°C and 7.5% CO_2. DRG neurons were plated with 0.3 µM Cytosine Arabinoside (AraC), 100 ng/ml NGF (Peptrotech) + brain-derived neurotrophic factor (BDNF; Peptrotech), and on days in vitro (DIV) 2 neurotrophins were reduced to 10 ng/ml NGF + BDNF with AraC and maintained until DIV6 for collection and lysis.

For compartmented Campenot chambers, 120,000 cells were plated in the CB compartment of a Teflon divider (Camp10; Tyler Research) attached to a p35 dish coated with Corning Matrigel GFR Membrane Matrix diluted in DMEM. DRG neurons were initially plated with 0.3 µM AraC, 100 ng/ml NGF + BDNF, and on DIV1 neurotrophins were reduced to 10 ng/ml NGF + BDNF with AraC only in the CB compartment. On DIV2, cultures were maintained in the same neurotrophin concentration (10 ng/ml for CB and 100 ng/ml for distal axons), but without AraC, and reduced to 0 ng/ml NGF + BDNF in the CB compartment and 1 ng/ml NGF + BDNF in the distal axon compartment with AraC from DIV5 to DIV8 for collecting protein lysates or for degeneration assay. As efficient knockdown of SFPQ with shRNA takes up to DIV8, the Campenot cultures used for degeneration assay involving shSFPQ were maintained until DIV12 with the following modifications: from DIV5 to DIV8, neurotrophins were maintained at 10 ng/ml NGF + BDNF for both CB and axons with AraC, then reduced to 1 ng/ml NGF + BDNF for both CB and axons with AraC until DIV12. In this study, we maintained a constant level of neurotrophins from day 8 to 12. This contrasts with the protocol used previously (Cosker et al., 2016) where we investigated the role of SFPQ in neurotrophin responses by analyzing axon viability following SFPQ knockdown in cells exposed to acute neurotrophin stimulation after a period of neurotrophin deprivation.

A microfluidic device with a 900-µm microgroove barrier XonaChip (XC900; Xona Microfluidics) was prepared for live cell imaging according to manufacturer's instructions, except following the PBS washes for XonaPDL (Xona Microfluidics) coating, the device was further incubated with 10 µg/ml laminin (Life Technologies) for 3 h at 37°C. The device was then washed with PBS and primed with DRG neuron medium until plating. In the CB compartment, 20,000 DRG neurons were plated to attach at room temperature for 5 min. DRG neurons were infected with lentivirus in the CB compartment diluted in media containing 0.3 µM AraC and 100 ng/ml NGF + BDNF. Fresh media with 0.3 µM AraC and 100 ng/ml NGF + BDNF was added to the distal axon compartment. At DIV1, virus was removed and replaced with fresh media in both compartments, with the CB neurotrophins reduced to 10 ng/ml NGF + BDNF with AraC and distal axon compartment with 0.3 µM AraC and 100 ng/ml NGF + BDNF. At DIV2, both CB and distal axon compartment were kept in 0.3 µM AraC and 5 ng/ml NGF + BDNF until live cell imaging at DIV5.

For immunofluorescence in microfluidic chambers, a silicon-based 450-µm microgroove barrier (SND450; Xona Microfluidics) was prepared following manufacturer's instructions with modifications. Sterilized cover glass was coated with 0.2 mg/ml poly-D-lysine (Sigma-Aldrich) overnight, then washed with water and dried. Microfluidic chambers were cleaned by briefly soaking in ethanol, then dried; attached onto PDL-coated glass slide; and the chambers and wells were filled with 10 µg/ml laminin and incubated for 3 h at 37°C. The chambers and wells were washed three times with neurobasal media, and 30,000 DRG neurons were plated in the CB compartment with 0.3 µM AraC and 50 ng/ml NGF + BDNF and in distal axon compartment with 0.3 µM AraC and 100 ng/ml NGF + BDNF. At DIV1, both compartments were replaced with fresh media, with 0.3 µM AraC and 10 ng/ml NGF + BDNF in the CB compartment and 0.3 µM AraC and 100 ng/ml NGF + BDNF in the distal axon compartment, and maintained until DIV5 for immunostaining. Fenstermacher et al. (2015) provides more details on compartmented culture system.

Immunofluorescence

DRG neurons grown in silicon-based microfluidic chambers were fixed with 4% PFA in PBS for 20 min at room temperature, then washed three times with PBS. The device was then carefully removed and cultures were then immediately permeabilized with 0.1% Triton X-100 in PBS for 10 min at room temperature and blocked for 1 h at room temperature with 3% BSA in PBS. KIF5 primary antibodies (1:100; Abcam) and mouse

TUJ1 antibodies (1:400; BioLegend) diluted in 3% BSA in PBS were incubated at 4°C overnight. Slides were washed three times with PBS and secondary antibodies diluted in 3% BSA in PBS (1:1,000; Invitrogen) were incubated for 1 h at RT. Finally, slides were washed two times with PBS and incubated with DAPI (1:1,000) in PBS, washed briefly, and mounted. Images were acquired with Nikon Ni-E C2 *Si* laser-scanning confocal microscope with a ×60 oil objective using NIS-Elements imaging software.

Axon degeneration assay

Compartmented chamber cultures were fixed at room temperature with 4% PFA diluted 1:2 in DRG neuron media for 10 min, then an additional 20 min in undiluted 4% PFA. DRGs were permeabilized with 0.1% Triton X-100 for 10 min, blocked in 3% BSA in 0.1% Triton X-100 for 1 h at room temperature, and incubated with rabbit anti-Tuj1 (1:400; BioLegend) overnight at 4°C. Cultures were then incubated with secondary antibodies (1:1,000; Invitrogen) for 1 h at room temperature and stained briefly with DAPI. Images of distal axon tips were obtained using a ×40 air objective, and axonal degeneration was quantified using the method described by Sasaki et al. (2009). TUJ1-stained images were binarized by using ImageJ to convert axonal areas to black and background areas to white. To detect fragmented (degenerating) axons, the particle analyzer function of ImageJ software was used (for total area we analyze particle size, 0-infinity; and for axon fragments, we set the particle size, 0–1,000). The degeneration index was calculated as the ratio of the area of fragmented axons over the total axon area. For peptide rescue experiment, the following peptides, synthesized as previously described (Barclay et al., 2015; Pease-Raissi et al., 2017), were used: Bclw BH4 SAHB$_A$ ALVADFVGYKLRXKGYXBGA and Bcl2 BH4 SAHB$_A$ EIVBKYIHYKLSXRGYXWDA (differential placement of all-hydrocarbon staples [X] along the BH4 sequences of Bclw and Bcl2; and B representing norleucine, replacing the native cysteine and methionine on Bclw and Bcl2, respectively).

The peptides were introduced into axons by using 2 µl Chariot protein transfection system (Active Motif) only in the distal axon compartment of compartmented Campenot chambers immediately after KIF5A^{R280H} virus removal at DIV2. The culture was kept with the peptides until DIV8 for axon degeneration assay.

Whole-mount immunostaining

Whole DRG with peripheral nerves were dissected from postnatal day 1 (P1) mice of either sex and fixed with 4% PFA at 4°C overnight. DRGs were washed in PBS, permeabilized in 0.5% Triton X-100 for 1 h, and blocked in 5% BSA and 0.5% Triton X-100 for 4 h. DRGs were incubated for 48 h in primary KIF5 (1:50; Abcam) and TUJ1 (1:300; BioLegend) antibodies at 4°C and washed overnight in PBS. DRGs were then incubated in secondary antibody (1:500; Life Technologies) at room temperature for 3.5 h. Images were acquired with Nikon Ni-E C2 Si laser-scanning confocal microscope with a ×40 oil objective.

Live cell imaging

DRGs neurons infected with lentivirus expressing Halo-SFPQ were grown in XonaChip microfluidic chambers and were labeled with tetramethylrhodamine Halo Tag ligand (Promega) according to the manufacturer's instructions with modifications. Tetramethylrhodamine stock was diluted in DRG culture medium at 1:200 and used at a final labeling concentration of 2.5 µM added to both CB and axon compartment. DRGs were incubated for 15 min at 37°C and washed three times with complete DRG culture medium made with neurobasal without phenol red and incubated for 30 min at 37°C to wash unbound ligand. DRG culture medium was replaced with low-fluorescence imaging media (HibernateE; Brain Bits) supplemented with 2% B27 and 1% GlutaMAX. DRG neurons were imaged live with a Nikon Ti-E in an environmental chamber at 37°C and 7.5% CO_2 using a ×60 oil 1.4 NA objective with a Perfect Focus System one frame every 1.5 s for 3 min in the most distal portion of the axons in the axonal compartment of microfluidic chambers. Due to various expression levels, neurons expressing easily visualizable puncta of Halo-SFPQ in axons were analyzed by using the Kymolyzer macro for ImageJ developed by the laboratory of Dr. Thomas Schwarz (Basu et al., 2020). To determine the SFPQ granule shape aspect ratio, the maximum and the minimum diameters of the granule were measured to get its ratio.

Western blot

HEK 293T cells or DRG sensory neurons were collected and prepared with lysis buffer (1% NP-40; 50 mM Tris-HCl, pH 7.4; 150 mM NaCl; 2 mM EDTA; protease inhibitor [Sigma-Aldrich]; and phosphatase inhibitor [Life Technologies]). Cell lysates were placed on ice for 20 min and centrifuged at 13,000 rpm for 20 min to collect the supernatant. Lysates were separated with 4–12% Bis-Tris NuPAGE gel (Thermo Fisher Scientific) and blotted with the following primary antibodies: mouse anti-SFPQ (1:1,000; Sigma-Aldrich), rabbit anti-KIF5A (1:2,000; Abcam), rabbit anti-KIF5B (1:2,000; Abcam), rabbit anti-KIF5C (1: 2,000; Abcam), rabbit anti-KIF3C (1:500; Abcam), rabbit anti-KIF3A (1:200; Abcam), rabbit anti-KIF1A (1:5,000; Abcam), mouse anti-Halo (1:1,000), rabbit anti-KLC1 (1:500; Santa Cruz Biotechnology), rabbit anti-KLC2 (1:1,000; Proteintech), rabbit anti-pan actin (1:1,000; Cell Signaling Technologies), mouse anti-Myc (1:500; Santa Cruz Biotechnology), mouse anti-FLAG (1:1,000; Sigma-Aldrich), mouse anti-HA (1:10,000; Thermo Fisher Scientific), and rabbit anti-GFP (1:2m000; Sigma-Aldrich). HRP-conjugated secondary antibodies (1:10,000; BioRad), ECL detection system (VWR International), and SuperSignal West Dura (Thermo Fisher Scientific) were used for chemiluminescent detection.

Transfection and immunoprecipitation

HEK 293T cells were cultured in a 10-cm plate with DMEM, 10% FBS (Thomas Scientific), and 1% penicillin/streptomycin at 37°C and 5% CO_2. For transfection, cells were plated in a 6-cm dish and, 24 h later, plasmids were transfected with Lipofectamine 2000 (Invitrogen) based on manufacturer's protocol, and then incubated for 24 h before immunoprecipitation experiments.

For immunoprecipitation, HEK 293T cells or DRG neurons were collected and lysed as described for Western blots, and 500 µg of protein lysate was precleared with 3 µl of Dynabeads protein G (Thermo Fisher Scientific) for 1 h (HEK 293T lysates) or 2 h (DRG neuron lysates) nutated at 4°C. For RNase experiments, the lysate was treated with RNase A/T1 (Thermo Fisher Scientific) for 1 h at room temperature and immediately immunoprecipitated. Following the manufacturer's instructions, protein lysate was immunoprecipitated for 2 h at 4°C with the following antibodies: rabbit anti-myc (2.5 µg; Millipore Sigma), mouse anti-HA (2.5 µg; Thermo Fisher Scientific), mouse anti-SFPQ (20 µg; Abcam), control normal mouse (Millipore Sigma), or normal rabbit IgG (Cell Signaling Technologies). The input—0.5% for HEK 293T and 3% for DRG—and the elute was analyzed with Western blot.

Lentivirus production and infection

HEK 293T cells grown on a 10-cm dish were transfected by using FuGENE 6 (Promega) with the transfer vector pxPAX2 (Addgene plasmid 12260) and pMD2.G (Addgene plasmid 12259), gifts from Didier Trono (École Polytechnique Fédérale de Lausanne, Lausanne, Switzerland), at a ratio of 4:3:1. The transfection reagent was replaced with fresh media after 24 h. Virus-containing media were collected 48 and 72 h after transfection, pooled, centrifuged at 1,200 rpm for 5 min, and filtered through a 0.45-µm polyethersulfone (PES) filter. Finally, the virus was concentrated by using Amicon ultra-15 centrifugal filter units (Sigma-Aldrich) and centrifuging at 3,000 rpm, the virus then being stored at −80°C until use. For infection of DRG sensory neurons, the virus was added at DIV1 for 24 h, except for XonaChip where virus was added immediately after plating. For experiments involving puromycin (Sigma-Aldrich) selection (Fig. 5, B and C, shSFPQ; Figs. 6 E and 7 F, WT and KIF5A^{R280H} constructs; Fig. S2 B, shKIF5A and shKIF5C), neurons were allowed to recover for 1 d after virus removal and 0.4 µg/ml puromycin was then added at DIV3 and replaced with fresh media at DIV5.

Quantitative RT-PCR

RNA for CB and distal axons were extracted from DRG neurons grown in Campenot compartmented cultures using TRIzol (Invitrogen) according to the manufacturer's protocol. Reverse transcription was performed by using the cDNA archive kit (Applied Biosystems) according to the manufacturer's protocol, and quantitative real-time RT-PCR was performed using Taqman Gene expression assays (Applied Biosystems). Expression levels of *bclw* (Rn00821025_g1) and *β actin* (Rn00667869_m1) were normalized to *gapdh* (Applied Biosystems).

Mitochondrial transport assay

DRGs neurons infected with lentivirus expressing puromycin-resistant HA-KIF5A, HA-KIF5A-R280H, and noninfected controls were grown in XonaChip microfluidic chambers. Puromycin-selected and control DRGs were labeled with MitoTracker Green FM according to manufacturer's instructions. MitoTracker Green FM stock was diluted in DRG culture medium at 1:10,000 and used at a final labeling concentration of 100 nM added to both CB and axon compartments. DRGs were incubated for 30 min at 37°C and washed three times with complete DRG culture medium made with neurobasal without phenol red. DRG culture medium was replaced with low-fluorescence imaging media (HibernateE; Brain Bits) supplemented with 2% B27 and 1% GlutaMAX. DRG neurons were imaged live with a Nikon Ti-E in an environmental chamber at 37°C and 7.5% CO_2 using a ×60 oil 1.4NA objective with a Perfect Focus System one frame every 1.5 s for 3 min in the most distal portion of axons in the axonal compartment of the microfluidic chambers. Mitochondrial transport in axons was analyzed by using the Kymolyzer macro for ImageJ developed by the laboratory of Dr. Thomas Schwarz (Basu et al., 2020).

Protein expression and purification

A construct of human KNS2 covering residues 205–501 in the pET28MHL vector, a gift from Cheryl Arrowsmith (University of Toronto, Toronto, Canada; Addgene plasmid 26096) was expressed in *Escherichia coli* BL21 (DE3) in Terrific Broth (TB) medium in the presence of 50 µg/ml kanamycin. Cells were grown at 37°C to an OD of 0.6, induced overnight at 17°C with 400 µM isopropyl-1-thio-D-galactopyranoside, collected by centrifugation, and stored at −80°C. Cell pellets were microfluidized at 15,000 psi in buffer A1 (25 mM Hepes [7.5], 500 mM NaCl, 5% glycerol, 30 mM Imidazole, 5 µM ZnAc, and 7 mM 2-Mercaptoethanol) and the resulting lysate was centrifuged at 13,000 rpm for 40 min. Ni-NTA beads (Qiagen) were mixed with lysate supernatant for 45 min, washed with buffer A1, and eluted with buffer Bi (25 mM Hepes [7.5], 500 mM NaCl, 5% glycerol, 400 mM Imidazole, 5 µM ZnAc, and 7 mM 2-Mercaptoethanol). The sample was gel-filtered through a Superdex-200 16/60 column in buffer A3 (20 mM Hepes [pH 7.5], 200 mM NaCl, 5% glycerol, 1 mM DTT, and 0.5 mM tris-(2-chloroethyl)-phosphate [TCEP]). Fractions were pooled, but protein began precipitating when concentrated. To combat apparent precipitation, excess NaCl solution was added to a final buffer composition of 18 mM Hepes (pH 7.5), 680 mM NaCl, 4.5% glycerol, 0.9 mM DTT, and 0.45 mM TCEP. The adjusted sample was then concentrated and stored at −80°C.

ITC

All calorimetric experiments were performed in 20 mM Hepes (pH 7.5), 150 mM NaCl, and 0.5 mM TCEP, with 2% DMSO at 25°C using an Affinity ITC from TA Instruments equipped with autosampler. Briefly, 350 µl of buffer or protein at 20 µM was placed into the calorimetric cell, and 250 µl of various SFPQ peptides (KE BioChem) at 200 µM were loaded into titration syringe. 4 µl syringe solution was injected into the calorimetric cell 30 times with a 200-s interval between injections. Thermodynamic parameters (K_d, stoichiometry, and enthalpy) were calculated according to the single-site model provided in NanoAnalyze software (TA Instruments).

Mass spectrometry (MS)

Antibody-conjugated protein A beads from KLC1 and SFPQ immunoprecipitates were suspended in 100 µl ammonium bicarbonate, reduced with 10 mM DTT for 30 min at 56°C, and alkylated with 20 mM iodoacetamide for 20 min at 22°C in the dark. Excess iodoacetamide was quenched by adding 10 mM DTT before diluting the samples to 250 µl with 100 mM ammonium bicarbonate. Immunoprecipitated proteins were digested overnight at 37°C with 4 µg trypsin. Tryptic peptides were desalted using 500 µg of a 1:1 mixture of hydrophobic and hydrophilic Sera-Mag Carboxylate-Modified Speed Beads (GE Healthcare Life Sciences).

Peptides were loaded onto a precolumn (100 µm × 4 cm POROS 10R2; Applied Biosystems) and eluted with a high-performance liquid chromatography gradient (NanoAcquity UPLC system; Waters; 1–40% B in 90 min; A = 0.2 M acetic acid in water, B = 0.2 M acetic acid in acetonitrile). Peptides were resolved on a self-packed analytical column (30 µm × 50 cm monitor C18; Column Engineering) and introduced in the mass spectrometer (QExactive HF mass spectrometer; Thermo Fisher Scientific) equipped with a Digital PicoView electrospray source platform (New Objective; Ficarro et al., 2009).

The mass spectrometer was programmed to perform a combination of targeted (parallel reaction monitoring [PRM]) and data-dependent tandem MS (MS/MS) scans. To select precursors for the PRM experiments, we first analyzed a small aliquot of digested KLC1 immunoprecipitate and selected the most intense precursor for peptides mapping uniquely to genes (Askenazi et al., 2010) that encode each protein of interest, further excluding peptides containing methionine residues. In data-dependent mode, the top five most abundant ions in each MS scan were subjected to collision-induced dissociation (higher-energy collisional dissociation; 27% normalized collision energy) MS/MS (isolation width = 1.5 D; intensity threshold = 1E5; max injection time: 50 ms). Dynamic exclusion was enabled with an exclusion duration of 30 s. PRM scans were scheduled across an 8-min period for each of the 45 precursors selected as described above (isolation width = 1.6 D; max injection time: 119 ms). ESI voltage was set to 3.8 kV.

MS spectra were recalibrated using the background ion (Si(CH3)2O)6 at m/z 445.12 ± 0.03 and converted into a Mascot generic file format (MGF) using multiplierz scripts (Alexander et al., 2017; Askenazi et al., 2009; Parikh et al., 2009). Spectra were searched using Mascot (version 2.6) against three appended databases consisting of: rat protein sequences (downloaded from UniProt on 04/09/2018), common laboratory contaminants, and a decoy database generated by reversing the sequences from these two databases. Precursor tolerance was set to 20 ppm and product ion tolerance to 25 mmu. Search parameters included trypsin specificity, up to two missed cleavages, fixed carbamidomethylation (C, +57 D), and variable oxidation (M, +16 D). Spectra matching to peptides from the reverse database were used to calculate a global false discovery rate and were discarded. Data were further processed to remove peptide spectral matches to the forward database with a false discovery rate > 1.0%.

The abundance of KIF5 and KLC family members in biochemical association with SFPQ was estimated by using a combination of quantitative label-free MS approaches. First, we sequentially analyzed KLC1 IP using data-dependent and targeted (PRM) liquid chromatography–MS/MS methods. Extracted ion chromatograms for the three most abundant peptide precursors from the data-dependent analysis (MS1-level scans) were used to estimate the abundance of KIF5A, KIF5B, KIF5C, KLC2, and KLC1 (Silva et al., 2006). Data from the PRM analysis (MS2-level scans) of the same KLC1 IP was used to calculate the summed intensity for the set of targeted precursor/fragment ions pairs selected for each protein (see previous section describing target selection). Combining these data enabled us to calculate conversion factors between intensities based on PRM analysis and extracted ion chromatogram–based abundance measured with the Top-3 approach. We then used the same PRM liquid chromatography MS/MS method to analyze three independent SFPQ IPs. We used the conversion factors calculated above to determine the abundance of KIF5A, KIF5B, KIF5C, KLC2, and KLC1. For clarity, we normalized these values to the most abundant member of each protein family, calculated as a percentage.

Quantification and statistical analysis

Data are expressed as mean ± SEM or SD. To assess statistical significance, data were analyzed with unpaired two-tailed Student's *t* test. For multiple comparisons, data were analyzed by one- or two-way ANOVA with Bonferroni or Dunnett's multiple comparison tests. Data distribution was assumed to be normal, but this was not formally tested. Significance was placed at $P < 0.05$. Statistical analysis was done using Microsoft Excel and GraphPad Prism.

Online supplemental material

Fig. S1 shows bioinformatic analysis of SFPQ protein sequence and transport parameters of SFPQ granules in axons of DRG sensory neurons. Fig. S2 shows KLC1 is phosphorylated and KIF5 motors differentially localize to CB and distal axons. Fig. S3 shows that the mode of SFPQ binding to KLC1 is distinct from JIP1. Fig. S4 shows transport parameters and shape aspect ratio for Halo-tagged WT and SFPQ^{Y527A}. Fig. S5 shows that mitochondrial transport is not altered by CMT-associated KIF5A^{R280H}. Video 1 and Video 2 show axonal transport of Halo-tagged SFPQ in axons of DRG sensory neurons. Data S1 summarizes data from liquid chromatography–MS/MS. Table S1 summarizes all reagents and resources used in this study.

Acknowledgments

We thank Thomas Schwarz and Himanish Basu (Boston Children's Hospital, Boston, MA) for Kymolyzer software. We also thank Gary Banker (Oregon Health and Science University, Portland, OR) and Marvin Bentley (Rensselaer Polytechnic Institute, Troy, NY) for the KIF5A, KIF5B, KIF5C, and KLC1 constructs; and Corinne Houart (Kings's College London, London, UK) for the SFPQ construct. We thank the Segal laboratory and Charles Stiles and Michael Greenberg for helpful comments on this manuscript.

This work was supported by National Institutes of Health grant K01NS110449 (to Y. Fukuda) and grant R01NS050674 (to R.A. Segal and J.A. Marto), as well as the Bertarelli Foundation Collaborative Award (to R.A. Segal and L.D. Walensky).

R.A. Segal: family member is on the board of directors for Allergen; scientific advisory board member for Amgen and Decibel Therapeutics. L.D. Walensky: stockholder in Aileron Therapeutics. J.A. Marto: receives sponsored research funding from Vertex and AstraZeneca and serves on the scientific advisory board of 908 Devices. The authors declare no further competing financial interests.

Author contributions: Y. Fukuda, M.F. Pazyra-Murphy, G. Adelmant, J.A. Marto, and R.A. Segal designed research. Y. Fukuda, M.F. Pazyra-Murphy, O.E. Tasdemir-Yilmaz, Y. Li, E.S. Silagi, L. Rose, Z.C. Yeoh, N.E. Vangos, E.A. Geffken, H.-S. Seo, and G. Adelmant performed experiments. Y. Fukuda, M.F. Pazyra-Murphy, E.S. Silagi, H.-S. Seo, S. Dhe-Paganon, G. Adelmant, and J.A. Marto analyzed data. G.H. Bird and L.D. Walensky provided reagents. Y. Fukuda and R.A. Segal wrote the paper with input from all other authors.

Submitted: 5 May 2020
Revised: 15 October 2020
Accepted: 6 November 2020

References

Alexander, W.M., S.B. Ficarro, G. Adelmant, and J.A. Marto. 2017. multiplierz v2.0: A Python-based ecosystem for shared access and analysis of native mass spectrometry data. *Proteomics.* 17:1700091. https://doi.org/10.1002/pmic.201700091

Askenazi, M., J.R. Parikh, and J.A. Marto. 2009. mzAPI: a new strategy for efficiently sharing mass spectrometry data. *Nat. Methods.* 6:240–241. https://doi.org/10.1038/nmeth0409-240

Askenazi, M., J.A. Marto, and M. Linial. 2010. The complete peptide dictionary--a meta-proteomics resource. *Proteomics.* 10:4306–4310. https://doi.org/10.1002/pmic.201000270

Barclay, L.A., T.E. Wales, T.P. Garner, F. Wachter, S. Lee, R.M. Guerra, M.L. Stewart, C.R. Braun, G.H. Bird, E. Gavathiotis, et al. 2015. Inhibition of Pro-apoptotic BAX by a noncanonical interaction mechanism. *Mol. Cell.* 57:873–886. https://doi.org/10.1016/j.molcel.2015.01.014

Basu, H., L. Ding, G. Pekkurnaz, M. Cronin, and T.L. Schwarz. 2020. Kymolyzer, a Semi-Autonomous Kymography Tool to Analyze Intracellular Motility. *Curr. Protoc. Cell Biol.* 87:e107. https://doi.org/10.1002/cpcb.107

Baumann, S., J. König, J. Koepke, and M. Feldbrügge. 2014. Endosomal transport of septin mRNA and protein indicates local translation on endosomes and is required for correct septin filamentation. *EMBO Rep.* 15:94–102. https://doi.org/10.1002/embr.201338037

Brady, S.T. 1985. A novel brain ATPase with properties expected for the fast axonal transport motor. *Nature.* 317:73–75. https://doi.org/10.1038/317073a0

Brenner, D., R. Yilmaz, K. Müller, T. Grehl, S. Petri, T. Meyer, J. Grosskreutz, P. Weydt, W. Ruf, C. Neuwirth, et al. German ALS network MND-NET. 2018. Hot-spot KIF5A mutations cause familial ALS. *Brain.* 141:688–697. https://doi.org/10.1093/brain/awx370

Campbell, P.D., K. Shen, M.R. Sapio, T.D. Glenn, W.S. Talbot, and F.L. Marlow. 2014. Unique function of Kinesin Kif5A in localization of mitochondria in axons. *J. Neurosci.* 34:14717–14732. https://doi.org/10.1523/JNEUROSCI.2770-14.2014

Carpentier, D.C., W.N. Gao, H. Ewles, G.W. Morgan, and G.L. Smith. 2015. Vaccinia virus protein complex F12/E2 interacts with kinesin light chain isoform 2 to engage the kinesin-1 motor complex. *PLoS Pathog.* 11: e1004723. https://doi.org/10.1371/journal.ppat.1004723

Cioni, J.-M., J.Q. Lin, A.V. Holtermann, M. Koppers, M.A.H. Jakobs, A. Azizi, B. Turner-Bridger, T. Shigeoka, K. Franze, W.A. Harris, et al. 2019. Late Endosomes Act as mRNA Translation Platforms and Sustain Mitochondria in Axons. *Cell* 176:56–72.e15.

Cosker, K.E., M.F. Pazyra-Murphy, S.J. Fenstermacher, and R.A. Segal. 2013. Target-derived neurotrophins coordinate transcription and transport of bclw to prevent axonal degeneration. *J. Neurosci.* 33:5195–5207. https://doi.org/10.1523/JNEUROSCI.3862-12.2013

Cosker, K.E., S.J. Fenstermacher, M.F. Pazyra-Murphy, H.L. Elliott, and R.A. Segal. 2016. The RNA-binding protein SFPQ orchestrates an RNA regulon to promote axon viability. *Nat. Neurosci.* 19:690–696. https://doi.org/10.1038/nn.4280

Courchesne, S.L., C. Karch, M.F. Pazyra-Murphy, and R.A. Segal. 2011. Sensory neuropathy attributable to loss of Bcl-w. *J. Neurosci.* 31:1624–1634. https://doi.org/10.1523/JNEUROSCI.3347-10.2011

Das, S., R.H. Singer, and Y.J. Yoon. 2019. The travels of mRNAs in neurons: do they know where they are going? *Curr. Opin. Neurobiol.* 57:110–116. https://doi.org/10.1016/j.conb.2019.01.016

Davidovic, L., X.H. Jaglin, A.M. Lepagnol-Bestel, S. Tremblay, M. Simonneau, B. Bardoni, and E.W. Khandjian. 2007. The fragile X mental retardation protein is a molecular adaptor between the neurospecific KIF3C kinesin and dendritic RNA granules. *Hum. Mol. Genet.* 16:3047–3058. https://doi.org/10.1093/hmg/ddm263

Diefenbach, R.J., J.P. Mackay, P.J. Armati, and A.L. Cunningham. 1998. The C-terminal region of the stalk domain of ubiquitous human kinesin heavy chain contains the binding site for kinesin light chain. *Biochemistry.* 37:16663–16670. https://doi.org/10.1021/bi981163r

Dutta, M., M.R. Diehl, J.N. Onuchic, and B. Jana. 2018. Structural consequences of hereditary spastic paraplegia disease-related mutations in kinesin. *Proc. Natl. Acad. Sci. USA.* 115:E10822–E10829. https://doi.org/10.1073/pnas.1810622115

Ebbing, B., K. Mann, A. Starosta, J. Jaud, L. Schöls, R. Schüle, and G. Woehlke. 2008. Effect of spastic paraplegia mutations in KIF5A kinesin on transport activity. *Hum. Mol. Genet.* 17:1245–1252. https://doi.org/10.1093/hmg/ddn014

Fenstermacher, S.J., M.F. Pazyra-Murphy, and R.A. Segal. 2015. Campenot cultures and microfluidics provide complementary platforms for spatial study of dorsal root ganglia neurons. *In* Microfluidic and Compartmentalized Platforms for Neurobiological Research: Neuromethods. Vol 103. E. Biffi, editor. Humana Press, New York. https://doi.org/10.1007/978-1-4939-2510-0_6

Ficarro, S.B., Y. Zhang, Y. Lu, A.R. Moghimi, M. Askenazi, E. Hyatt, E.D. Smith, L. Boyer, T.M. Schlaeger, C.J. Luckey, and J.A. Marto. 2009. Improved electrospray ionization efficiency compensates for diminished chromatographic resolution and enables proteomics analysis of tyrosine signaling in embryonic stem cells. *Anal. Chem.* 81:3440–3447. https://doi.org/10.1021/ac802720e

Füger, P., V. Sreekumar, R. Schüle, J.V. Kern, D.T. Stanchev, C.D. Schneider, K.N. Karle, K.J. Daub, V.K. Siegert, M. Flötenmeyer, et al. 2012. Spastic paraplegia mutation N256S in the neuronal microtubule motor KIF5A disrupts axonal transport in a Drosophila HSP model. *PLoS Genet.* 8: e1003066. https://doi.org/10.1371/journal.pgen.1003066

Hewage, T.W., S. Caria, and M. Lee. 2019. A new crystal structure and small-angle X-ray scattering analysis of the homodimer of human SFPQ. *Acta Crystallogr. F Struct. Biol. Commun.* 75:439–449. https://doi.org/10.1107/S2053230X19006599

Hirokawa, N., S. Niwa, and Y. Tanaka. 2010. Molecular motors in neurons: transport mechanisms and roles in brain function, development, and disease. *Neuron.* 68:610–638. https://doi.org/10.1016/j.neuron.2010.09.039

Hirose, T., T. Yamazaki, and S. Nakagawa. 2019. Molecular anatomy of the architectural NEAT1 noncoding RNA: The domains, interactors, and biogenesis pathway required to build phase-separated nuclear paraspeckles. *Wiley Interdiscip. Rev. RNA.* 10:e1545. https://doi.org/10.1002/wrna.1545

Holt, C.E., K.C. Martin, and E.M. Schuman. 2019. Local translation in neurons: visualization and function. *Nat. Struct. Mol. Biol.* 26:557–566. https://doi.org/10.1038/s41594-019-0263-5

Huang, C.F., and G. Banker. 2012. The translocation selectivity of the kinesins that mediate neuronal organelle transport. *Traffic.* 13:549–564. https://doi.org/10.1111/j.1600-0854.2011.01325.x

Huang, E.J., and L.F. Reichardt. 2001. Neurotrophins: roles in neuronal development and function. *Annu. Rev. Neurosci.* 24:677–736. https://doi.org/10.1146/annurev.neuro.24.1.677

Jacobson, C., B. Schnapp, and G.A. Banker. 2006. A change in the selective translocation of the Kinesin-1 motor domain marks the initial specification of the axon. *Neuron.* 49:797–804. https://doi.org/10.1016/j.neuron.2006.02.005

Jennings, S., M. Chenevert, L. Liu, M. Mottamal, E.J. Wojcik, and T.M. Huckaba. 2017. Characterization of kinesin switch I mutations that cause hereditary spastic paraplegia. *PLoS One.* 12:e0180353. https://doi.org/10.1371/journal.pone.0180353

Kanai, Y., Y. Okada, Y. Tanaka, A. Harada, S. Terada, and N. Hirokawa. 2000. KIF5C, a novel neuronal kinesin enriched in motor neurons. *J. Neurosci.* 20:6374–6384. https://doi.org/10.1523/JNEUROSCI.20-17-06374.2000

Kanai, Y., N. Dohmae, and N. Hirokawa. 2004. Kinesin transports RNA: isolation and characterization of an RNA-transporting granule. *Neuron.* 43:513–525. https://doi.org/10.1016/j.neuron.2004.07.022

Knowles, R.B., J.H. Sabry, M.E. Martone, T.J. Deerinck, M.H. Ellisman, G.J. Bassell, and K.S. Kosik. 1996. Translocation of RNA granules in living neurons. *J. Neurosci.* 16:7812–7820. https://doi.org/10.1523/JNEUROSCI.16-24-07812.1996

Krauss, R., T. Bosanac, R. Devraj, T. Engber, and R.O. Hughes. 2020. Axons Matter: The Promise of Treating Neurodegenerative Disorders by Targeting SARM1-Mediated Axonal Degeneration. *Trends Pharmacol. Sci.* 41:281–293. https://doi.org/10.1016/j.tips.2020.01.006

Lipka, J., L.C. Kapitein, J. Jaworski, and C.C. Hoogenraad. 2016. Microtubule-binding protein doublecortin-like kinase 1 (DCLK1) guides kinesin-3-mediated cargo transport to dendrites. *EMBO J.* 35:302–318. https://doi.org/10.15252/embj.201592929

Liu, Y.T., M. Laurá, J. Hersheson, A. Horga, Z. Jaunmuktane, S. Brandner, A. Pittman, D. Hughes, J.M. Polke, M.G. Sweeney, et al. 2014. Extended phenotypic spectrum of KIF5A mutations: From spastic paraplegia to axonal neuropathy. *Neurology.* 83:612–619. https://doi.org/10.1212/WNL.0000000000000691

Luisier, R., G.E. Tyzack, C.E. Hall, J.S. Mitchell, H. Devine, D.M. Taha, B. Malik, I. Meyer, L. Greensmith, J. Newcombe, et al. 2018. Intron retention and nuclear loss of SFPQ are molecular hallmarks of ALS. *Nat. Commun.* 9:2010. https://doi.org/10.1038/s41467-018-04373-8

Miki, H., M. Setou, K. Kaneshiro, and N. Hirokawa. 2001. All kinesin superfamily protein, KIF, genes in mouse and human. *Proc. Natl. Acad. Sci. USA.* 98:7004–7011. https://doi.org/10.1073/pnas.111145398

Nakajima, K., X. Yin, Y. Takei, D.H. Seog, N. Homma, and N. Hirokawa. 2012. Molecular motor KIF5A is essential for GABA(A) receptor transport, and KIF5A deletion causes epilepsy. *Neuron.* 76:945–961. https://doi.org/10.1016/j.neuron.2012.10.012

Nakata, T., and N. Hirokawa. 2003. Microtubules provide directional cues for polarized axonal transport through interaction with kinesin motor head. *J. Cell Biol.* 162:1045–1055. https://doi.org/10.1083/jcb.200302175

Nam, D.E., D.H. Yoo, S.S. Choi, B.O. Choi, and K.W. Chung. 2018. Wide phenotypic spectrum in axonal Charcot-Marie-Tooth neuropathy type 2 patients with KIF5A mutations. *Genes Genomics.* 40:77–84. https://doi.org/10.1007/s13258-017-0612-x

Nguyen, T.Q., M. Aumont-Nicaise, J. Andreani, C. Velours, M. Chenon, F. Vilela, C. Geneste, P.F. Varela, P. Llinas, and J. Ménétrey. 2018. Characterization of the binding mode of JNK-interacting protein 1 (JIP1) to kinesin-light chain 1 (KLC1). *J. Biol. Chem.* 293:13946–13960. https://doi.org/10.1074/jbc.RA118.003916

Nicolas, A., K.P. Kenna, A.E. Renton, N. Ticozzi, F. Faghri, R. Chia, J.A. Dominov, B.J. Kenna, M.A. Nalls, P. Keagle, et al. 2018. Genome-wide Analyses Identify KIF5A as a Novel ALS Gene. *Neuron* 97:1268-1283.e6.

Nussbacher, J.K., R. Tabet, G.W. Yeo, and C. Lagier-Tourenne. 2019. Disruption of RNA Metabolism in Neurological Diseases and Emerging Therapeutic Interventions. *Neuron.* 102:294–320. https://doi.org/10.1016/j.neuron.2019.03.014

Parikh, J.R., M. Askenazi, S.B. Ficarro, T. Cashorali, J.T. Webber, N.C. Blank, Y. Zhang, and J.A. Marto. 2009. multiplierz: an extensible API based desktop environment for proteomics data analysis. *BMC Bioinformatics.* 10:364. https://doi.org/10.1186/1471-2105-10-364

Pease-Raissi, S.E., M.F. Pazyra-Murphy, Y. Li, F. Wachter, Y. Fukuda, S.J. Fenstermacher, L.A. Barclay, G.H. Bird, L.D. Walensky, and R.A. Segal. 2017. Paclitaxel Reduces Axonal Bclw to Initiate IP3R1-Dependent Axon Degeneration. *Neuron* 96:373-386.e6.

Pernigo, S., M.S. Chegkazi, Y.Y. Yip, C. Treacy, G. Glorani, K. Hansen, A. Politis, S. Bui, M.P. Dodding, and R.A. Steiner. 2018. Structural basis for isoform-specific kinesin-1 recognition of Y-acidic cargo adaptors. *eLife.* 7:e38362. https://doi.org/10.7554/eLife.38362

Randall, T.S., C. Moores, and F.A. Stephenson. 2013. Delineation of the TRAK binding regions of the kinesin-1 motor proteins. *FEBS Lett.* 587:3763–3769. https://doi.org/10.1016/j.febslet.2013.09.049

Sahoo, P.K., D.S. Smith, N. Perrone-Bizzozero, and J.L. Twiss. 2018. Axonal mRNA transport and translation at a glance. *J. Cell Sci.* 131:jcs196808. https://doi.org/10.1242/jcs.196808

Salvadores, N., M. Sanhueza, P. Manque, and F.A. Court. 2017. Axonal Degeneration during Aging and Its Functional Role in Neurodegenerative Disorders. *Front. Neurosci.* 11:451. https://doi.org/10.3389/fnins.2017.00451

Sasaki, Y., B.P. Vohra, F.E. Lund, and J. Milbrandt. 2009. Nicotinamide mononucleotide adenylyl transferase-mediated axonal protection requires enzymatic activity but not increased levels of neuronal nicotinamide adenine dinucleotide. *J. Neurosci.* 29:5525–5535. https://doi.org/10.1523/JNEUROSCI.5469-08.2009

Setou, M., D.H. Seog, Y. Tanaka, Y. Kanai, Y. Takei, M. Kawagishi, and N. Hirokawa. 2002. Glutamate-receptor-interacting protein GRIP1 directly steers kinesin to dendrites. *Nature.* 417:83–87. https://doi.org/10.1038/nature743

Silva, J.C., M.V. Gorenstein, G.Z. Li, J.P. Vissers, and S.J. Geromanos. 2006. Absolute quantification of proteins by LCMSE: a virtue of parallel MS acquisition. *Mol. Cell. Proteomics.* 5:144–156. https://doi.org/10.1074/mcp.M500230-MCP200

Sleigh, J.N., A.M. Rossor, A.D. Fellows, A.P. Tosolini, and G. Schiavo. 2019. Axonal transport and neurological disease. *Nat. Rev. Neurol.* 15:691–703. https://doi.org/10.1038/s41582-019-0257-2

Tanaka, Y., S. Niwa, M. Dong, A. Farkhondeh, L. Wang, R. Zhou, and N. Hirokawa. 2016. The Molecular Motor KIF1A Transports the TrkA Neurotrophin Receptor and Is Essential for Sensory Neuron Survival and Function. *Neuron.* 90:1215–1229. https://doi.org/10.1016/j.neuron.2016.05.002

Tas, R.P., A. Chazeau, B.M.C. Cloin, M.L.A. Lambers, C.C. Hoogenraad, and L.C. Kapitein. 2017. Differentiation between Oppositely Oriented Microtubules Controls Polarized Neuronal Transport. *Neuron* 96: 1264-1271.e5.

Thomas-Jinu, S., P.M. Gordon, T. Fielding, R. Taylor, B.N. Smith, V. Snowden, E. Blanc, C. Vance, S. Topp, C.H. Wong, et al. 2017. Non-nuclear Pool of Splicing Factor SFPQ Regulates Axonal Transcripts Required for Normal Motor Development. *Neuron.* 94:931. https://doi.org/10.1016/j.neuron.2017.04.036

Vale, R.D., T.S. Reese, and M.P. Sheetz. 1985. Identification of a novel force-generating protein, kinesin, involved in microtubule-based motility. *Cell.* 42:39–50. https://doi.org/10.1016/S0092-8674(85)80099-4

Verhey, K.J., D. Meyer, R. Deehan, J. Blenis, B.J. Schnapp, T.A. Rapoport, and B. Margolis. 2001. Cargo of kinesin identified as JIP scaffolding proteins and associated signaling molecules. *J. Cell Biol.* 152:959–970. https://doi.org/10.1083/jcb.152.5.959

Wang, B., L. Pan, M. Wei, Q. Wang, W.W. Liu, N. Wang, X.Y. Jiang, X. Zhang, and L. Bao. 2015. FMRP-Mediated Axonal Delivery of miR-181d Regulates Axon Elongation by Locally Targeting Map1b and Calm1. *Cell Rep.* 13:2794–2807. https://doi.org/10.1016/j.celrep.2015.11.057

Xia, Ch., A. Rahman, Z. Yang, and L.S. Goldstein. 1998. Chromosomal localization reveals three kinesin heavy chain genes in mouse. *Genomics.* 52: 209–213. https://doi.org/10.1006/geno.1998.5427

Xu, M., Y. Gu, J. Barry, and C. Gu. 2010. Kinesin I transports tetramerized Kv3 channels through the axon initial segment via direct binding. *J. Neurosci.* 30:15987–16001. https://doi.org/10.1523/JNEUROSCI.3565-10.2010

Yamazaki, T., S. Souquere, T. Chujo, S. Kobelke, Y.S. Chong, A.H. Fox, C.S. Bond, S. Nakagawa, G. Pierron, and T. Hirose. 2018. Functional Domains of NEAT1 Architectural lncRNA Induce Paraspeckle Assembly through Phase Separation. *Mol. Cell,* 70:1038-1053.e7.

Yoon, B.C., H. Jung, A. Dwivedy, C.M. O'Hare, K.H. Zivraj, and C.E. Holt. 2012. Local translation of extranuclear lamin B promotes axon maintenance. *Cell.* 148:752–764. https://doi.org/10.1016/j.cell.2011.11.064

Zhao, J., A.H.K. Fok, R. Fan, P.Y. Kwan, H.L. Chan, L.H. Lo, Y.S. Chan, W.H. Yung, J. Huang, C.S.W. Lai, and K.O. Lai. 2020. Specific depletion of the motor protein KIF5B leads to deficits in dendritic transport, synaptic plasticity and memory. *eLife.* 9:e53456. https://doi.org/10.7554/eLife.53456

Zhu, H., H.Y. Lee, Y. Tong, B.S. Hong, K.P. Kim, Y. Shen, K.J. Lim, F. Mackenzie, W. Tempel, and H.W. Park. 2012. Crystal structures of the tetratricopeptide repeat domains of kinesin light chains: insight into cargo recognition mechanisms. *PLoS One.* 7:e33943. https://doi.org/10.1371/journal.pone.0033943

Supplemental material

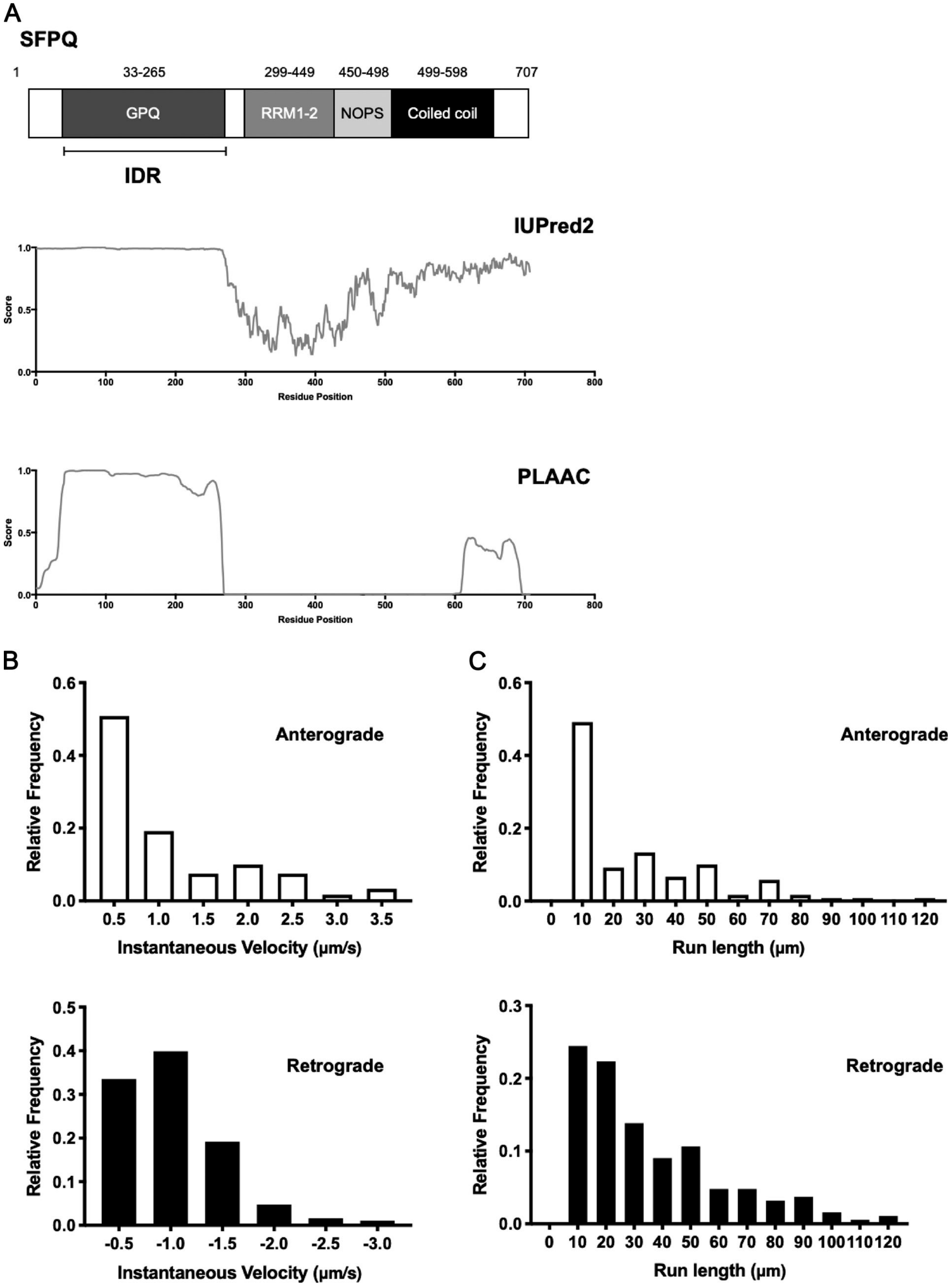

Figure S1. **Bioinformatic analysis of SFPQ protein sequence and transport parameters of SFPQ granules in axons of DRG sensory neurons. (A)** Schematic of protein domains of SFPQ and the probability score of the SFPQ sequence for being disordered and prion like as predicted by IUPred2 (top) and PLAAC (bottom), respectively. **(B and C)** Frequency distribution of instantaneous velocity (A) and run length (B) for Fig. 1, E and F, respectively. Data analyzed from 259 SFPQ particles, from 34 axons across four independent microfluidic experiments. IDR, intrinsically disordered region.

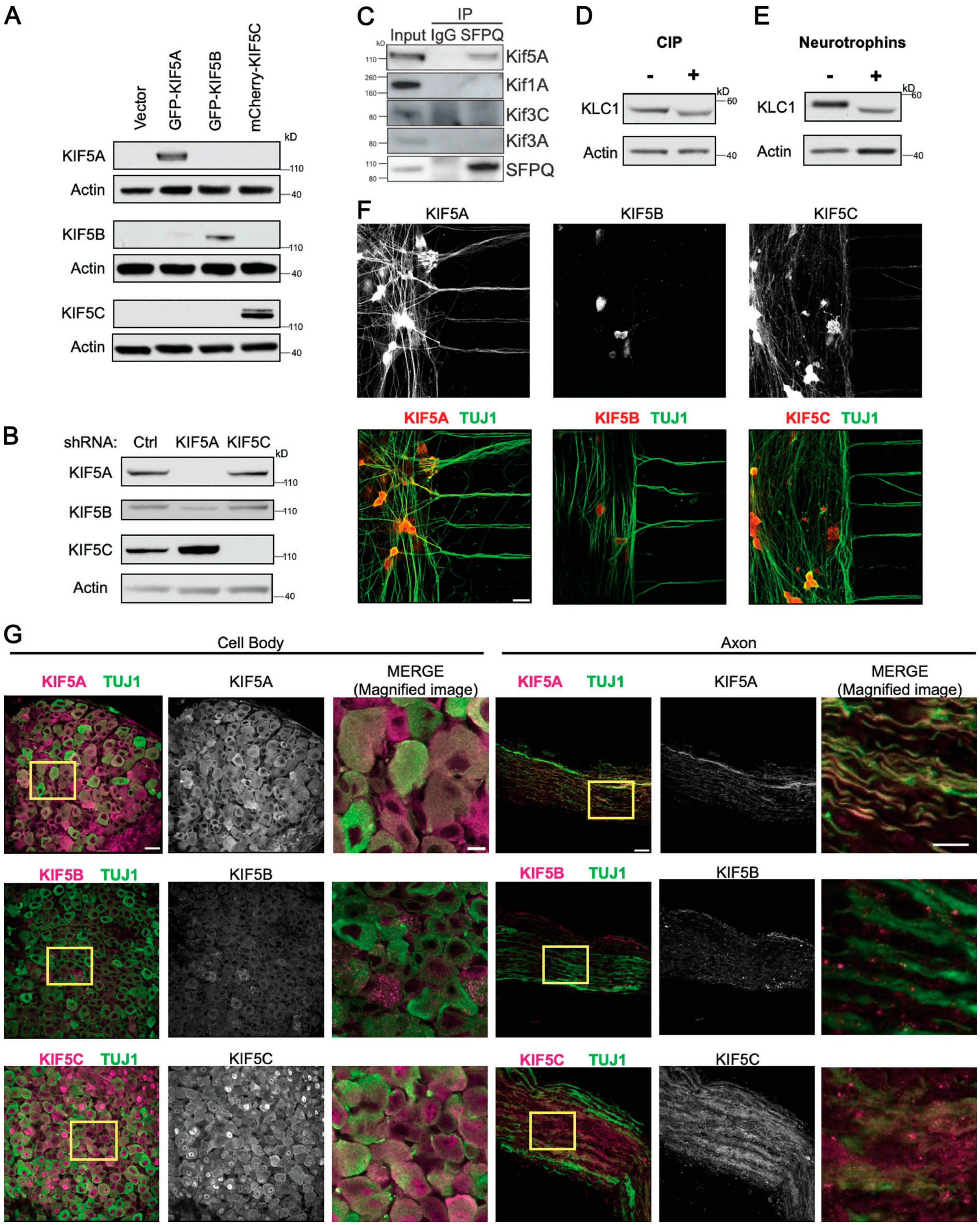

Figure S2. **KLC1 is phosphorylated and KIF5 motors differentially localize to CB and distal axons. (A)** Western blot of HEK 293T cells transfected with empty vector, GFP-KIF5A, GFP-KIF5B, or mCherry-KIF5C and probed with the KIF5 antibodies. Actin serves as loading control. **(B)** DRG sensory neurons infected with control (Ctrl) or with either shRNA against *KIF5A* or *KIF5C* and probed with the KIF5 antibodies. Actin serves as loading control. **(C)** IP of endogenous SFPQ from DRG sensory neuron protein lysate and blotted against endogenous KIF5A, KIF1A, KIF3C, and KIF3A. IgG serves as control IP, input represents 3% of 0.5 mg of protein lysate used for SFPQ IP, and total elute from the bead was run on the gel. **(D)** DRG protein lysates were treated with intestinal alkaline phosphatase (CIP) and blotted against KLC1. Actin serves as loading control. **(E)** Lysates of DRG neuronal cultures maintained in neurotrophins or starved were blotted for KLC1. Actin serves as loading control. **(F)** Staining of endogenous KIF5A, KIF5B, and KIF5C in DRG sensory neurons grown in microfluidic chambers. Scale bar 20 µm; TUJ1 (green), KIF5 (red). **(G)** Staining of endogenous KIF5A, KIF5B, and KIF5C in DRGs and sciatic nerve of post-natal day 1 (P1) mice; *n* = 4 independent staining of tissues; scale bar: 30 µm and 9 µm for unmagnified images and merge magnified images, respectively; Tuj1 (green), KIF5 (magenta).

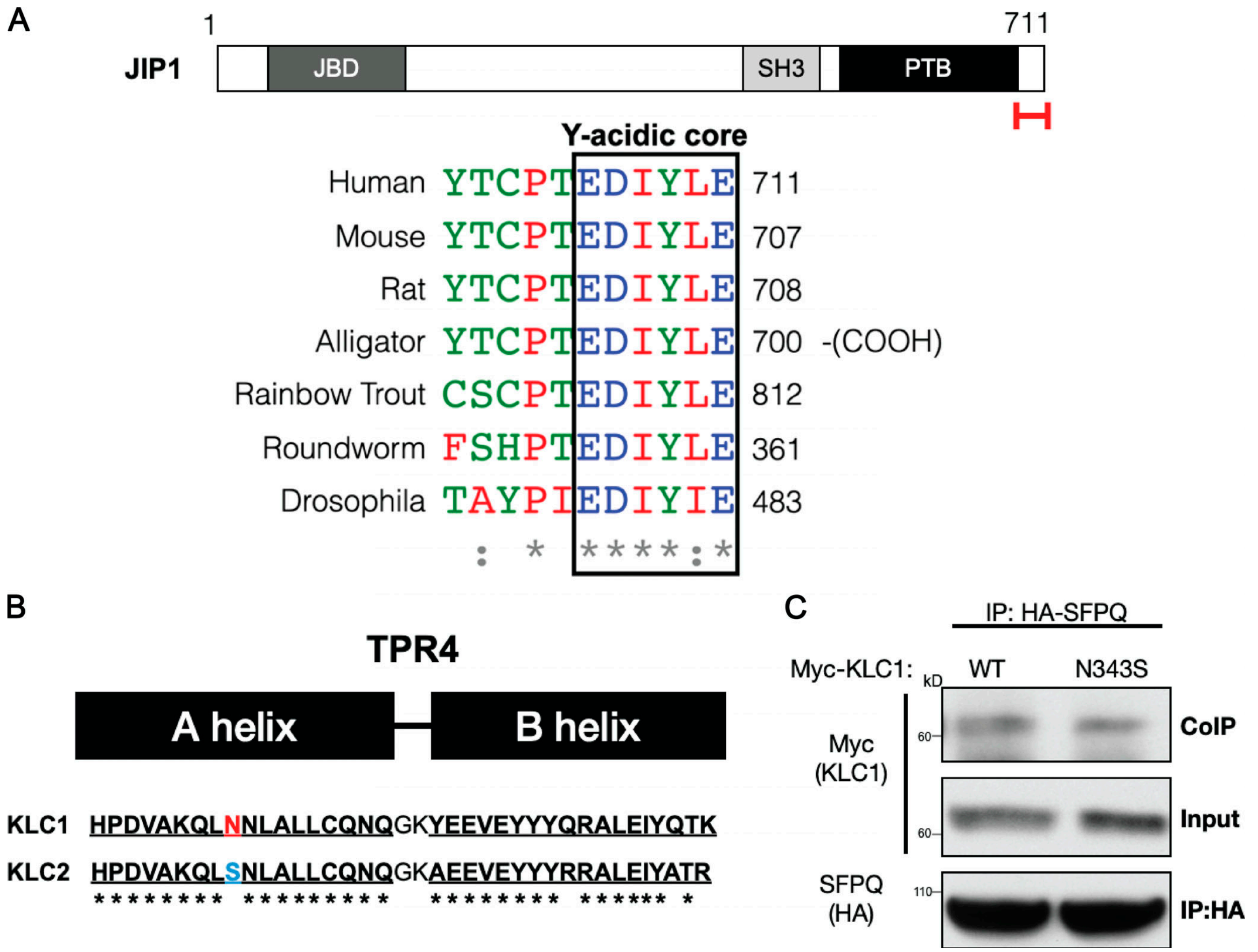

Figure S3. **SFPQ mode of binding to KLC1 is distinct from JIP1. (A)** Alignment of the sequence within the C-terminal region of JIP1 containing the Y-acidic motif. Bottom: Schematic of the domains of JIP1. Red bracket indicates the region containing the Y-acidic motif. **(B)** Schematic cartoon depicting the location of N343 on KLC1 compared with KLC2 on the A helix of TPR4. **(C)** HEK 293T cells transfected with HA-SFPQ, and with either Myc-tagged WT KLC1 or KLC1^{N343S}. HA was immunoprecipitated and blotted against HA and Myc. Input represents 0.5% of 0.5 mg of protein lysate used for HA IP, and total elute from the bead was run on the gel. JBD, JNK binding domain; PTB, phosphotyrosine binding domain; SH3, Src homology-3 domain.

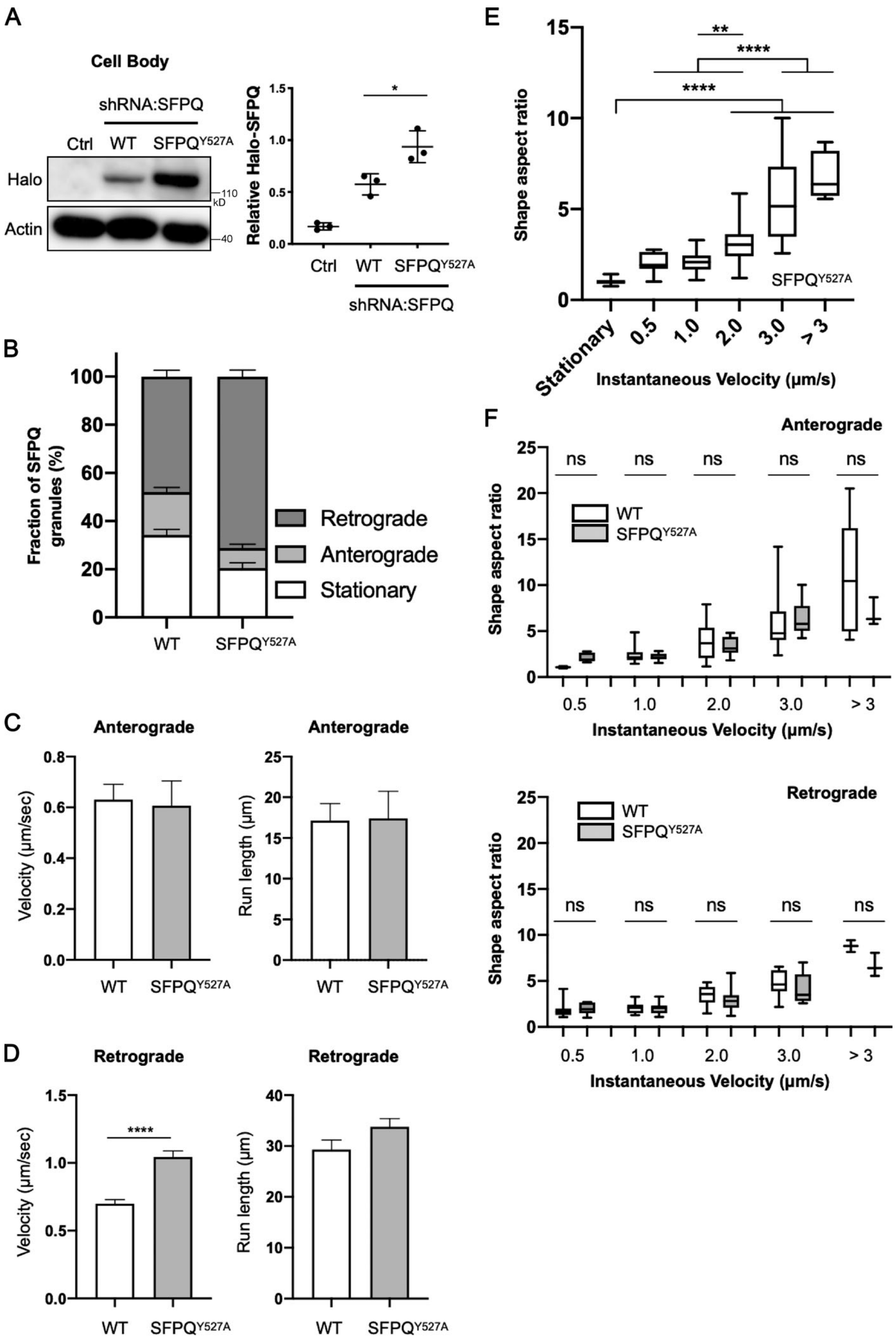

Figure S4. **Transport parameters and shape aspect ratio for Halo-tagged WT and SFPQ^{Y527A}. (A)** Left: Expression levels of Halo-tagged WT and SFPQ^{Y527A} in CB compartment from neurons simultaneously infected with shRNA against endogenous SFPQ. Neurons were grown in Campenot compartmented cultures and CB lysate was collected. Actin serves as loading control (Ctrl). Right: Relative Halo-SFPQ (normalized to actin) is quantified. *P = 0.0149; data are from three independent experiments; data represent mean ± SEM. **(B)** Percentage of time spent in stationary, anterograde, or retrograde phase for WT and SFPQ^{Y527A}. **(C)** Average anterograde velocity and run length for WT and SFPQ^{Y527A}. **(D)** Average retrograde velocity and run length for WT and SFPQ^{Y527A}. ****P < 0.0001. Data from B–D are analyzed from 258 granules for WT control and 202 granules for SFPQ^{Y527A} from at least 30 axons across at least four independent microfluidic experiments. **(E)** Shape aspect ratio (maximum diameter/minimum diameter) of SFPQ^{Y527A} granules calculated for stationary and moving granules, categorized with their instantaneous velocities as indicated. Data are calculated from 15 SFPQ granules from five axons from three independent microfluidic experiments for time points in stationary (*n* = 14), ≤0.5 (*n* = 14), 0.5–1 (*n* = 28), 1–2 (*n* = 48), 2–3 (*n* = 24), and >3 µm/s (*n* = 6). ****P < 0.0001; **P = 0.0061 by one-way ANOVA. **(F)** Comparison of shape aspect ratio between WT SFPQ and SFPQ^{Y527A} granules moving in anterograde (top) or retrograde transport (bottom). Data for WT anterograde granules are calculated from six SFPQ granules from five axons from five independent microfluidic experiments for time points in ≤0.5 (*n* = 5), 0.5–1 (*n* = 12), 1–2 (*n* = 12), 2–3 (*n* = 13), and >3 µm/s (*n* = 9). Retrograde: Data are calculated from 15 SFPQ granules from five axons from five independent microfluidic experiments for time points in ≤0.5 (*n* = 28), 0.5–1 (*n* = 17), 1–2 (*n* = 16), 2–3 (*n* = 12), and >3 µm/s (*n* = 2). Data for SFPQ^{Y527A} anterograde granules are calculated from six SFPQ granules from two axons from two independent microfluidic experiments for time points in ≤0.5 (*n* = 8), 0.5–1 (*n* = 12), 1–2 (*n* = 22), 2–3 (*n* = 13), and >3 µm/s (*n* = 3). Retrograde: Data are calculated from eight SFPQ granules from three axons from three independent microfluidic experiments for time points in ≤0.5 (*n* = 6), 0.5–1 (*n* = 16), 1–2 (*n* = 26), 2–3 (*n* = 11), and >3 µm/s (*n* = 3).

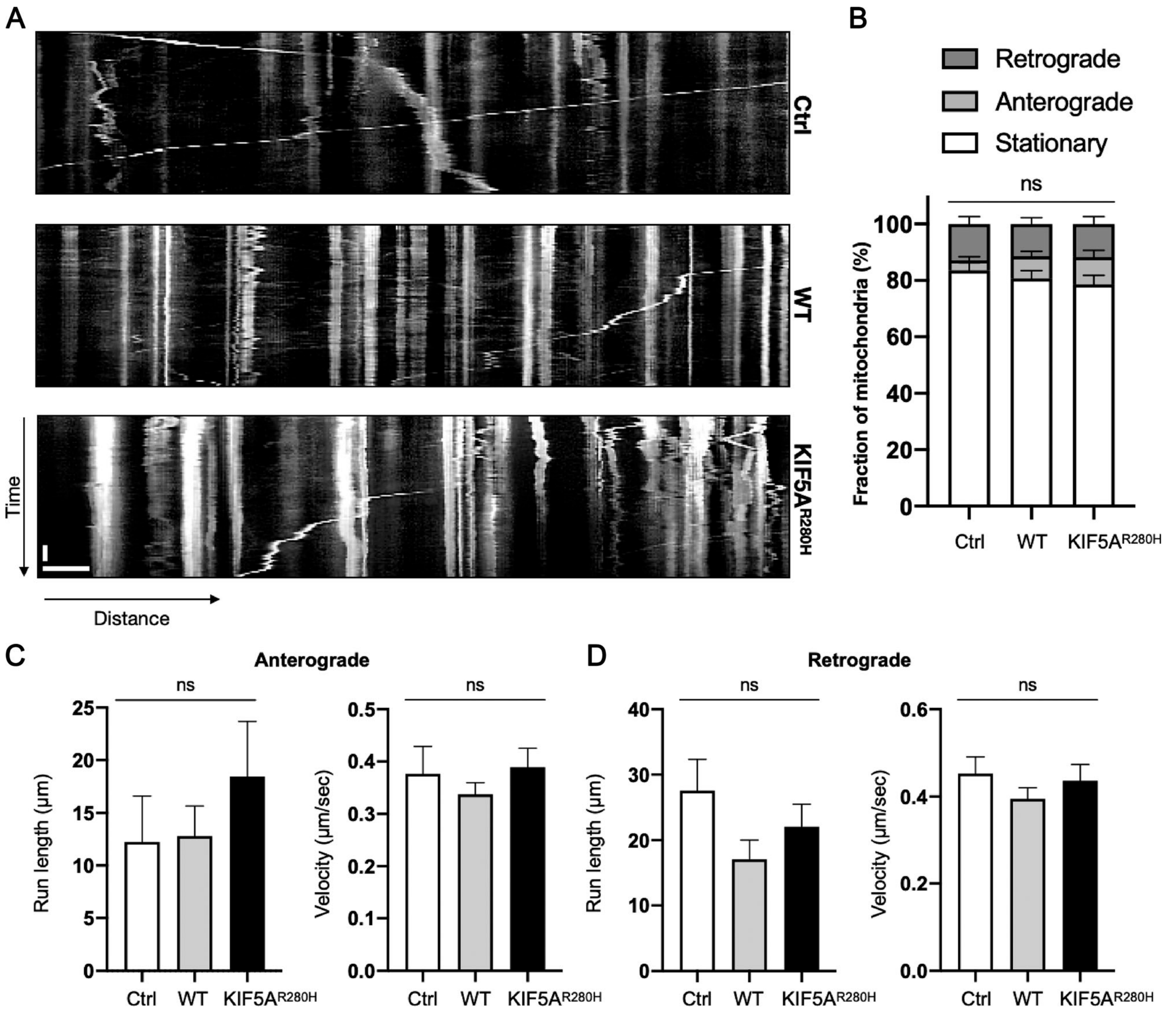

Figure S5. **Mitochondrial transport is not altered by CMT-associated KIF5A^{R280H}. (A)** Kymograph of mitochondrial transport in axons of control (Ctrl), WT KIF5A-expressing, and KIF5A^{R280H}-expressing DRG neurons. Scale bars: 6 µm and 15 s. **(B)** Fraction of mitochondria spent in stationary, anterograde, or retrograde phase in control, WT KIF5A-expressing, and KIF5A^{R280H}-expressing DRGs. **(C and D)** Average run length and velocity of mitochondrial in axons of control, WT KIF5A-expressing, and KIF5A^{R280H}-expressing DRGs in C anterograde and D retrograde transport. Data represent mean ± SEM. Data from B–D were analyzed from ~115 mitochondria from 10 axons across three independent microfluidic experiments.

Video 1. **Halo-SFPQ is transported in anterograde and retrograde manner in axons.** Time-lapse movie was captured in axons of DRG sensory neurons grown in microfluidic compartmented cultures. The video is 135 s, was acquired every 1.5 s, and is played at 10 frames per second.

Video 2. **SFPQ^{Y527A} mutation disrupts axonal transport of SFPQ.** Time-lapse movie was captured in axons of DRG sensory neurons grown in microfluidic compartmented cultures. The video is 180 s, was acquired every 1.5 s, and is played at 10 frames per second.

Provided online as a Word file is Table S1, which summarizes all reagents and resources used in this study. A dataset is also provided online as an Excel file. Data S1 summarizes data from liquid chromatography–MS/MS.